



HAL
open science

Life-cycle performance prediction and interpretation for coastal and marine RC structures: An ensemble learning framework

Hongyuan Guo, You Dong, Emilio Bastidas-Arteaga, Xiaoming Lei

► To cite this version:

Hongyuan Guo, You Dong, Emilio Bastidas-Arteaga, Xiaoming Lei. Life-cycle performance prediction and interpretation for coastal and marine RC structures: An ensemble learning framework. *Structural Safety*, 2024, 110, pp.102496. 10.1016/j.strusafe.2024.102496 . hal-04620181

HAL Id: hal-04620181

<https://hal.science/hal-04620181v1>

Submitted on 21 Jun 2024

HAL is a multi-disciplinary open access archive for the deposit and dissemination of scientific research documents, whether they are published or not. The documents may come from teaching and research institutions in France or abroad, or from public or private research centers.

L'archive ouverte pluridisciplinaire **HAL**, est destinée au dépôt et à la diffusion de documents scientifiques de niveau recherche, publiés ou non, émanant des établissements d'enseignement et de recherche français ou étrangers, des laboratoires publics ou privés.

Please cite this paper as: Guo, H., Dong, Y., Bastidas-Arteaga, E., & Lei, X. (2024). Life-cycle performance prediction and interpretation for coastal and marine RC structures: An ensemble learning framework. *Structural Safety*, 110, 102496. <https://doi.org/10.1016/j.strusafe.2024.102496>

Life-cycle performance prediction and interpretation for coastal and marine RC structures: An ensemble learning framework

Hongyuan Guo¹, You Dong¹, Emilio Bastidas-Arteaga², Xiaoming Lei^{1,1}

¹ Department of Civil and Environmental Engineering, Hong Kong Polytechnic University, Hong Kong, 999077, China.

² Laboratory of Engineering Sciences for the Environment (LaSIE - UMR CNRS 7356), La Rochelle University, La Rochelle, France.

Abstract: Long-term exposure to coastal and marine environments accelerates the aging of reinforced concrete (RC) structures, impacting their structural safety and society impact. Traditional assessments of long-term performance deterioration in RC structures involve complex, nonlinear, and time-intensive studies of physical mechanisms. While existing machine learning (ML) methods can assess the lifetime of these structures, they often prioritize data regression over mechanistic interpretation. To enhance the efficiency and interpretability of predicting the life-cycle performance of RC structures, this study introduces a generic framework based on interpretable ensemble learning (EL) methods. The framework predicts life-cycle performance efficiently and accurately, with optimal hyperparameters automatically tuned through Bayesian optimization. Interpretability algorithms clarify the influence of environmental, durability, and mechanical parameters on structural durability and mechanical predictions. Validation employs real-world cases of RC hollow beams in the coastal area of the Guangdong-Hong Kong-Macao Greater Bay Area (GBA). The comprehensive model for RC structures integrates actual data on temperature, humidity, and surface chloride content in the GBA, considering diffusion, convection, and binding effects of chloride ions, corrosion non-uniformity, and crack impact on durability estimation. Comparative analysis with existing ML methods underscores the effectiveness of the framework. The findings highlight the dynamic evolution of feature importance rankings throughout the service life, shedding light on the continuous changes in the significance of different factors when predicting mechanical resistance.

Keywords: RC structures; Corrosion; Marine exposure; Life-cycle performance; Ensemble learning; Interpretable models

1. Introduction

The long-term performance of reinforced concrete (RC) structures is susceptible to environmental actions, such as chloride ingress and concrete carbonation, which will impact structural functionality and safety, and even lead to significant societal and environmental consequences [1,2]. Among the environmental challenges confronting RC structures,

¹ Corresponding Author (E-mail: xiaoming.lei@polyu.edu.hk)

reinforcement corrosion emerges as a pivotal concern [3]. According to a report by Det Norske Veritas (DNV), the global cost of corrosion reached an estimated \$25 trillion, equivalent to 3.4% of the global GDP in 2013 [4]. In Western Europe, the annual expenditure for repairing corrosion-induced damage amounts to 500 million euros [5]. Given the substantial damage inflicted by reinforcement corrosion, it is imperative to investigate its impact on RC structure performance and conduct comprehensive life-cycle assessments for these structures. Thus, a profound understanding of concrete performance is crucial for accurately estimating the durability and service life of these structures.

Over the years, researchers have delved deeply into the mechanisms and theories studies relating to reinforcement corrosion, utilizing probabilistic approaches to assess the life-cycle performance of marine concrete structures [6,7]. For instance, Stewart *et al.* [8] and Wang *et al.* [9] have proposed a probabilistic method for evaluating corrosion damage to explore the effects of climate change on corrosion-induced damage in Australia. However, their studies adopted a simplified performance prediction approach, wherein only the diffusion mechanisms of corrosive media were considered. Besides, Guo *et al.* [10] proposed a performance-based durability assessment framework that integrates the effects of uncertainties with the chloride transport model, taking into account the impact of global warming on the life-cycle performance and complicated transport and impact mechanisms of chloride ions. Moreover, considering that RC structures may retain residual loading capacity and reliability even after reinforcement corrosion, Bastidas-Arteaga [11] elaborated on the impact of global warming on the limit state-based reliability of RC bridge structures under chloride ingress, considering limit states alongside durability assessments. In the realm of probabilistic assessment methods, conventional techniques like Monte Carlo simulation (MCS) have been widely applied but are accompanied by a notable computational burden [7,12]. To enhance efficiency without compromising precision, Guo *et al.* [1,13–15] have conducted a series of studies using the probability density function informed method (PDFM) for the prediction of deterioration and reliability analysis of the life cycle performance of RC structures under realistic environmental effects. Although PDFM has proven to be efficient, it is fundamentally a sampling-based approach, lacking in generalizability. Therefore, to enhance the efficiency of probabilistic assessment of the life-cycle performance of RC structures, there is still a need to develop more generalized and versatile methods.

Given the limitations and challenges posed by traditional methods in predicting the life-cycle performance of RC structures, there has been a notable shift toward the utilization of machine learning (ML). This shift is attributed to ML's ability to model the intricate physical processes inherent in lifetime assessment [16–18]. For instance, Fu and Feng [16] developed an ML-based method to predict the remaining shear strength of corroded RC beams. Additionally, Zhang *et al.* [19] used time-based artificial neural networks to perform probabilistic assessments of the structural capacity of corroded RC structures based on randomly generated samples of crack widths and corrosion-induced steel weight loss. However, it is worth noting that the realm of ML encompasses a variety of algorithms, and it is not a one-size-fits-all solution. ML algorithms exhibit adaptability and limitations within civil engineering [20]. Consequently, there remains a necessity to develop tailored and efficient ML algorithms that align with the physical processes governing the life-cycle performance evolution of deteriorating RC structures.

Ensemble learning (EL) emerges as a highly effective strategy for amalgamating multiple individual ML learners to create more accurate surrogate models. While individual ML models have showcased their predictive capabilities in previous studies, EL stands out for its capacity to generalize and alleviate the risk of overfitting [21–23]. For instance, Feng *et al.* [24] employed ensemble methods to predict the shear capacity of RC beams, surpassing mechanics-driven approaches in terms of accuracy. Their findings underscored the superior performance of EL methods. Similarly, Kiani *et al.* [25] utilized the random forest model, a form of EL employing a bagging algorithm, to develop seismic fragility models. Their research demonstrated the model's exceptional efficiency in forecasting seismic responses, both on balanced and imbalanced datasets. In a study by Hwang *et al.* [26], boosting algorithms within EL exhibited the highest performance when predicting responses and classifying failures in modern code-compliant RC frame buildings. Furthermore, Xu *et al.* [27] conducted a comprehensive comparison of various single and ensemble learning methods to construct a seismic assessment model for corroded RC columns. Their results conclusively favored the ensemble learning model as the most adept at predicting seismic failure modes. By leveraging the predictions of individual learners in an averaged or sequential manner, ensemble learning methods have the potential to significantly enhance the predictive performance of data-driven models.

With the growing popularity of data-driven techniques in the field of civil engineering [28–30], there is a growing recognition that the lack of interpretability inherent in these models poses a significant challenge in understanding the rationale behind their specific predictions. In response to this challenge, researchers have been actively exploring techniques to explain data-driven models, aiming to quantify the impact of input features on their predictions. Recent studies have seen numerous researchers employing explainable ML methods to gain insights into and predict structural performance. For instance, Feng *et al.* [31] assessed the significance of individual features in the prediction of shear strength for squat-reinforced concrete walls. Lei *et al.* [32] interpreted the effects of load responses on bridges using structural health monitoring data, quantifying the influence of critical loads on the displacement of girders and pylons. Their research included a comprehensive comparison of three prevalent interpretation techniques, outlining their respective advantages and disadvantages. Additionally, Wakjira *et al.* [34] pioneered the development of a surrogate model for estimating the plastic hinge length of RC columns, introducing an approach designed to elucidate the model's outcomes.

This study endeavors to tackle the computationally intensive nature of physical models when assessing the life-cycle performance of RC structures. The approach involves introducing an interpretable EL method aimed at creating an efficient data-driven surrogate model to predict the life-cycle performance of these structures. Optimization of the surrogate model's optimal hyperparameters and parameters is automated through Bayesian optimization. This robust model demonstrates superior predictive capabilities for critical life-cycle performance of RC structures based on input physical and environmental parameters (e.g., exposure condition and chloride ingress), outperforming alternative data-driven models. The training of the EL-based surrogate model incorporates considerations for structural uncertainties and diverse environmental characteristics within the dataset. Additionally, an interpretation algorithm is integrated to elucidate the influence of input features on the model's predictions, including the effects on global warming. The contributions of this study are provided as follows: 1) A comprehensive

environmental and durability assessment model for RC structures in Greater Bay Area (GBA) was established, validated, and investigated in terms of actual experimental records. 2) An efficient and accurate prediction model for the life-cycle performance of RC structures is formulated using LightGBM, and its optimal hyperparameters are automatically tuned through Bayesian optimization. 3) The interpretability algorithms are employed to clarify the influence of environmental, durability, and mechanical parameters on structural durability and mechanical predictions from diverse perspectives. The findings highlight the dynamic evolution of feature importance rankings throughout the service life, shedding light on the continuous changes in the significance of different factors when predicting mechanical resistance.

The structure of this paper is outlined as follows: Section 2 introduces the proposed framework, presenting the fundamental steps and details of the case under investigation. Section 3 delves into the essential algorithms of EL. Furthermore, Sections 4 and 5 elaborate the time-variant performance assessment physical model and corresponding modeling performance of EL model. Section 6 offers an in-depth discussion of the analysis results concerning the established model. Finally, the conclusions from the study are drawn in Section 7, and their life-cycle performance can be predicted and understood more wisely using the proposed method.

2. Life-cycle performance prediction and interpretation framework

This study developed a concise three-step framework to evaluate the life-cycle performance of RC structures, covering both structural durability and mechanical properties (Fig. 1). In Step 1, case-specific data is collected, and models for performance deterioration are formulated and validated, with detailed procedures outlined in Section 4. Step 2 involves addressing uncertainties through probabilistic analysis and Latin Hypercube sampling (LHS) for dataset generation, as explained in Section 5.1. Finally, in Step 3, surrogate modeling is refined using Bayesian optimization with the generated samples, with further elaboration provided in Section 3.

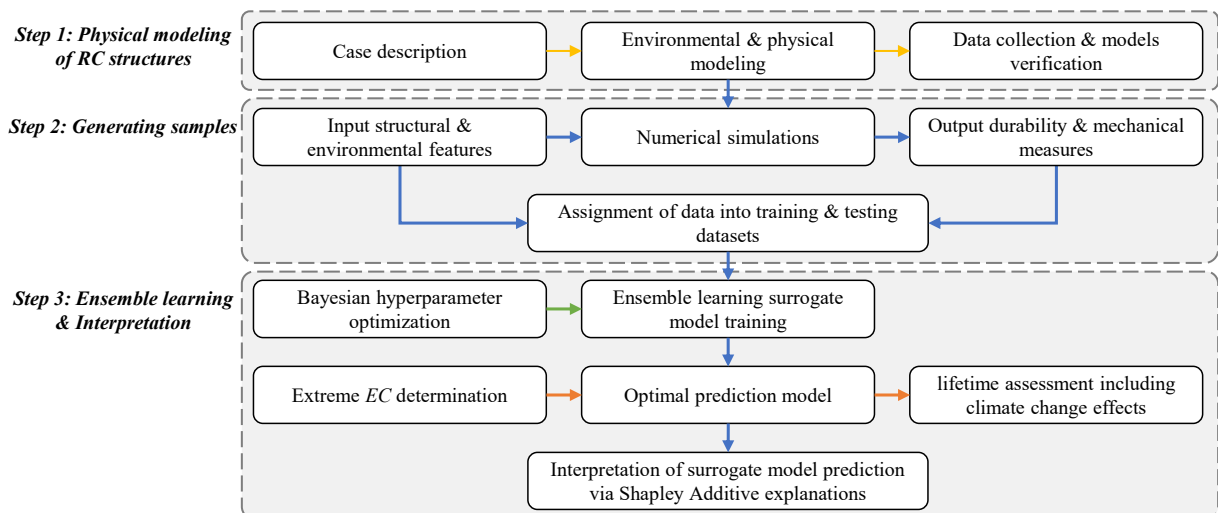


Fig. 1 Flowchart of ML model-based prediction and interpretation

To exemplify the framework, data from a typical RC bridge is utilized, illustrating how the methodology predicts life-cycle performance deterioration (Section 4). It is worth emphasizing that RC beam bridges represent complex structures with intricate geometries and material

interactions. Achieving accurate physics-based predictions for such structures entails a substantial investment of computational resources and analysis time with the comprehensive consideration of various influencing factors. Limited numerical simulations provide crucial datasets for training surrogate models. Once validated, these models effectively forecast durability and mechanical responses at different service life stages using untrained test datasets. By incorporating feature values over time intervals, the model ensures precise predictions of variations in life-cycle performance.

3. Ensemble learning-based predictive and interpretable methods

3.1 LightGBM surrogate ensemble learning model

Various data-driven models exist for regression problems, with EL offering effective methods, particularly in ML. EL's core concept involves amalgamating predictions from diverse models, with bagging and boosting pivotal for enhancing ML models. LightGBM, a tree-based EL technique, harnesses the strengths of multiple models to improve predictive accuracy. XGBoost [23], a popular and potent ML algorithm belonging to the gradient boosting methods family, has been widely adopted. CatBoost, tailored for categorical features, is another notable gradient boosting library. While deep learning models excel in regression tasks, their intricate structures and lack of interpretability can cause challenges, especially in large datasets with high-dimensional features. A general comparison of these algorithms is depicted in Fig. 2. In addressing the life-cycle performance prediction of coastal and marine RC structures, among various EL and deep learning models, LightGBM is adopted by considering its swift speed, minimal memory usage, high accuracy, and interpretability [28,29].









Comparison of state-of-the-art model	Ensemble learning			Deep learning
	 LightGBM	 XGBoost	 Yandex CatBoost	
Speed/Scalability	Fast 	Fast	Moderate	Moderate
Training consumption	Low 	Moderate	High	High
Accuracy	High 	High	High	High
Blackbox	No 	No	No	Yes

Fig. 2 Comparison of state-of-the-art models for data prediction

The foundational component of LightGBM is the decision tree (DT), denoted as f_{DT} . Decision trees use simple decision rules to capture data correlations, represented as:

$$f_{DT}(x) = \sum_{n=1}^N c_n I(x \in R_n) \quad (1)$$

where x represents the input feature; $I(\cdot)$ is the indicator function; c_n is the prediction outcome from the n -th leaf node; and R_n represents the N input subspaces.

LightGBM stands out through its unique tree construction and optimization approach, particularly adept at handling high-dimensional and sparse data. Employing Gradient-based One-Side Sampling (GOSS) streamlines training by prioritizing instances crucial for gradient updates, enhancing efficiency. Exclusive Feature Bundling (EFB) further improves efficacy by

consolidating correlated features, reducing feature count without sacrificing accuracy. This technique addresses challenges in high-dimensional data, resulting in accelerated training and enhanced model performance. Leaf value determination employs least squares optimization, incorporating gradient (Eq. (2)) and Hessian (Eq.(3)) calculations. This optimization process plays a pivotal role in achieving accurate and robust model predictions.

$$G_i = \partial L(y_i, F(x_i)) / \partial F(x_i) \quad (2)$$

$$H_i = \partial^2 L(y_i, F(x_i)) / (\partial F(x_i))^2 \quad (3)$$

$$\gamma_i = -G_i / (H_i + \lambda) \quad (4)$$

where G_i is the gradient of the loss function with respect to the predicted value $F(x_i)$ for the i -th sample; $L(y_i, F(x_i))$ is the loss function comparing true label y_i with predicted value $F(x_i)$ for the i -th sample; H_i represents the Hessian of the loss function with respect to the predicted value $F(x_i)$ for the i -th sample; γ_i denotes the optimal value for the i -th leaf node; and λ is the regularization parameter controlling tree complexity.

Moreover, LightGBM allows flexibility through parameter customization and model interpretation. Tuning options control model complexity, boosting processes, and regularization. The model supports interpretability techniques such as feature importance analysis and decision tree visualization, facilitating a deeper understanding of the learned model.

3.2 Tree-based Shapley Additive explanations

This study addresses the persistent challenge of interpreting predictions in ML algorithms, focusing on enhancing the interpretability of life-cycle performance predictions generated by LightGBM surrogate models. The proposed framework incorporates SHAP (SHapley Additive exPlanations) to quantify contributions of input physical and environmental features to model predictions, fostering a comprehensive understanding of individual feature impacts on overall outcomes [30].

The primary objective of SHAP is to offer explanations for predictions on a per-data-instance basis, assessing the influence of each feature on that specific prediction. By modeling features as a linear system, SHAP defines the feature vector, denoted as x' , which encompasses all characteristic values for a given data instance x . This enables SHAP to provide explanations for each prediction, elucidating the significance and role of each feature in shaping the model's decision process. The explanation model, $g(\cdot)$, can be represented as follows:

$$g(x') = \varphi_0 + \sum_{i=1}^M \varphi_i \quad (5)$$

where M is the maximum feature size; and $\varphi_i \in \mathbb{R}$ denotes the contribution of feature i .

SHAP exhibits efficiency, symmetry, and additivity, akin to Shapley values, along with three crucial properties: local accuracy, missingness, and consistency. Specifically,

1) local accuracy measures how closely the explanations provided by the model align with the outcomes of the initial ML model. Such a relationship can be depicted as:

$$\hat{f}(\mathbf{x}') = g(\mathbf{x}') = \varphi_0 + \sum_{i=1}^M \varphi_i \mathbf{x}'_i \quad (6)$$

where $\varphi_0 = E_X(\hat{f}(\mathbf{X}))$; φ_0 is the base value, representing the expected value of the model output when all feature values are set to their reference values. $\sum_{i=1}^M \varphi_i \mathbf{x}'_i$ accounts for the contribution of each feature to the estimated output.

2) Missingness ensures that the contribution of a missing feature is zero. This property mandates that missing features possess a Shapley value of zero; and

3) The consistency property asserts that if changes are made to the model, the Shapley value will also increase or decrease at the same extent.

Given the computational efficiency and predictive performance of tree-based SHAP, and LightGBM algorithm belonging to tree-based models, this study employs tree-based SHAP for computing Shapley values and determining feature contributions.

4. Environmental, durability and mechanical modeling

This section provides an in-depth account of environmental, durability, and mechanical models for RC structures in marine environments, incorporating experimental validations. Fig. 3 encapsulates essential procedures and models, with a specific emphasis on durability estimation (corrosion rate and concrete cracking width) and mechanical behavior estimation (residual flexural capacity M_{res} over the service life, considering non-linear properties of concrete and corroded steel bars).

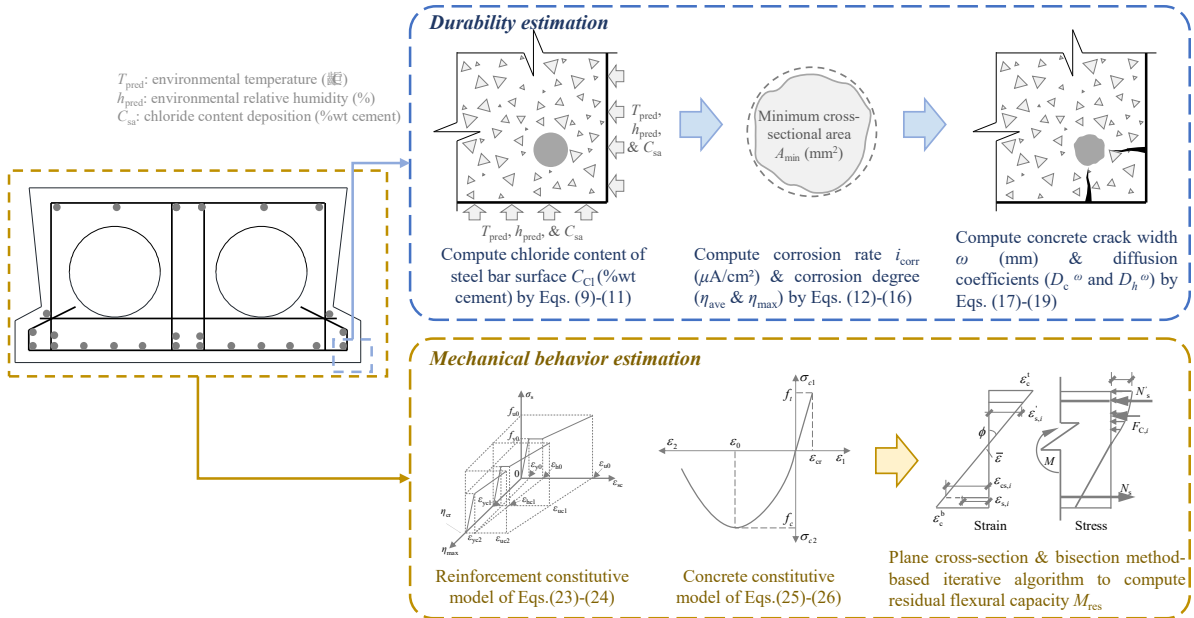


Fig. 3 Schematic for estimating durability and mechanical performance

4.1 Case description: RC hollow beams

Hollow beam bridges, characterized by a hollow cross-section (e.g., box or tubular shapes), are commonly employed for small to medium spans, offering advantages like increased stiffness, reduced material usage, and easy maintenance. In China, approximately 50% of the small and

middle-span bridge highway network consists of these structures, emphasizing the need for a detailed examination of their life-cycle performance [31].

This study focuses on recently constructed reinforced concrete bridges within a one-kilometer radius along the Greater Bay Area (GBA) coastline in China, with a specific emphasis on those completed in 2020. The investigation concentrates on the midsections of hollow beam bridges with three distinct spans (6, 8, 10 m, Fig. 4), recommended by the Ministry of Transportation as design references. Considering the longitudinal cross-sectional loss, the corrosion non-uniformity factor R is introduced to predict the minimum cross-sectional area loss of longitudinal bars [7]. When it comes to the transverse direction, the results depend on the considered transport mode. For one-dimensional transport, it is assumed that all steel bars undergo a consistent area loss. In two-dimensional transport, the area losses of steel bars are contingent upon their positions. In this study, steel bars situated at the section corners are assumed to exhibit the same corrosion degrees, while those positioned at non-corner locations are likewise presumed to have the same corrosion degrees.

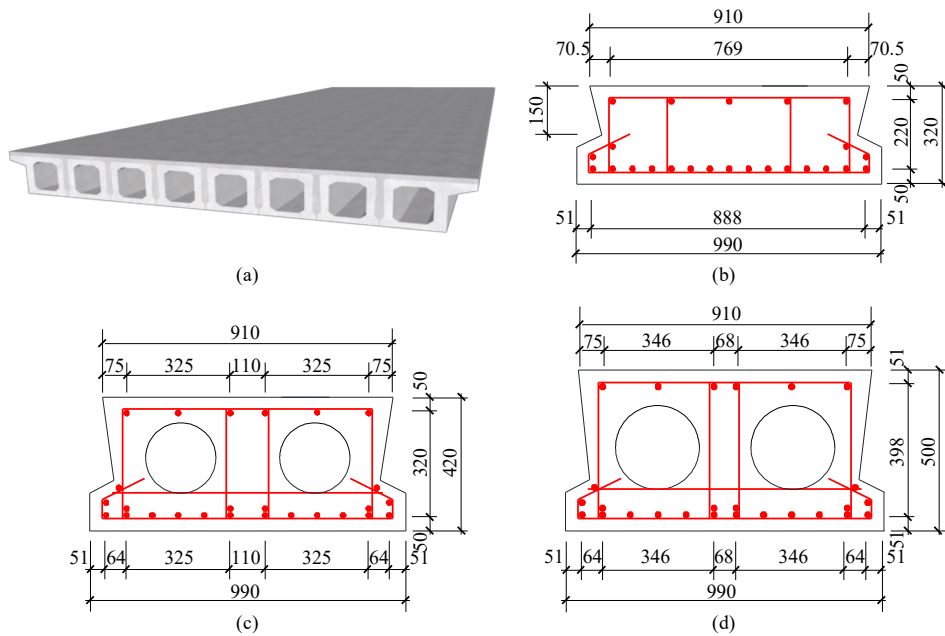


Fig. 4 (a) Schematic of RC hollow beam; (b) cross-section of 6 m span beam; (c) cross-section of 8 m span beam; and (d) cross-section of 10 m span beam

Table 1 summarizes key input and output parameters for the life-cycle performance assessment of these sections. Input parameters encompass facets related to the environment, durability, and mechanical behaviors of RC hollow beams, while output parameters consist of chloride content, corrosion degree, and residual mechanical capacities. This comprehensive assessment serves as a robust method to depict their overall condition and behavior.

Table 1 Input and output parameters of interest

Input features	Output measures
Concrete resistivity R_c	Free chloride content of steel bar surface C_{fc}
Reference chloride diffusion coefficient $D_{c,ref}$	Total chloride content of steel bar surface C_{tc}
Critical chloride content c_{cr}	Average corrosion degree of tensile bars $\eta_{ave,ten}$
Characteristic value of exposure condition (EC)	Average corrosion degree of compression bars $\eta_{ave,com}$
Critical corrosion degree η_{cr}	Maximum corrosion degree of tensile bars $\eta_{max,ten}$
Corrosion non-uniformity R_0	Maximum corrosion degree of compression bars $\eta_{max,com}$
Yield strength of steel bar f_{y0}	Residual bending capacity M_{res}
Elastic modulus of steel bar E_{s0}	
Concrete compressive strength f_c	
Elastic modulus of concrete E_{cs}	

Furthermore, Table 2 and Table 3 detail concrete mixtures and reinforcement layouts for various beam spans, and Table 4 provides input variable distribution details. It is assumed here that all random inputs in Table 4 are mutually independent random variables. Further research is required to characterize the correlation between the considered random variables and therefore improve the reliability assessment. Random variables will be used for probabilistic life-cycle performance evaluation using the models in the subsequent sections. Sections 0 - 4.4 elaborate on the adopted environmental model, durability, and mechanical behavior assessment. It is essential to note that, though many models are involved in life cycle assessment [1,7,10,12,32–40], these models primarily serve an illustrative purpose in this study. Nevertheless, this study diverges from previous studies which often rely solely on simplistic analytical models [41–43], by incorporating the finite difference method (FDM) and iterative computational procedures for load capacity calculations of corroded RC beams. Therefore, compared to most existing studies, the models used in this study better capture the temporal and stochastic variations of changing environments, as well as the nonlinearities and uncertainties of material properties. Furthermore, with the exception of the environmental and chloride transport models, which would be validated using in-situ experimental records (as detailed in Sections 0 and 4.3.1), other models pertaining to the corrosion propagation stage and mechanical assessment are either based on regression modeling in terms of experimental data or have been corroborated in prior studies.

Table 2 Mixture proportion of concrete

w/c	Water(kg/m3)	Cement (kg/m3)	Sand(kg/m3)	Aggregate (kg/m3)	Admixture (kg/m3)
0.4	181.7	454.3	704.1	1058.5	1.4

Table 3 Reinforcement schemes for different beam spans

Span (m)	Tension bar		Compression bar	
	Diameter d_0 (mm)	Number	Diameter d_0 (mm)	Number
6	18	15, 2	10	5
8	18	12, 6	16	6
10	20	12, 6	17	6

Note: Two numbers of steel bars mean there are two rows of steel bars.

Table 4 Random variables and corresponding distribution information

Parameter (unit)	Description	Distribution	Mean	COV (coefficient of variation)	Ref.
$D_{c, \text{ref}}$ (m ² /s)	Reference diffusion coefficient	Lognormal	6×10^{-12}	0.1	[10]
c_{cr} (%wt cement)	Critical chloride content	Lognormal	0.4	0.25	[11]
R_c (Ohms)	Resistance of cover concrete	Lognormal	1×10^4	0.1	[44]
f_{y0} (MPa)	Yield strength of steel bar	Normal	500	0.1	[45]
E_{s0} (MPa)	Elastic modulus of steel bar	Normal	2.73×10^5	0.05	[46]
f_c (MPa)	Compressive strength of concrete	Normal	40	0.2	[47]
E_{cs} (MPa)	Elastic modulus of concrete	Normal	3.20×10^4	0.1	[47]

4.2 Environmental model

In this section, temperature and relative humidity (*RH*) predictions are performed using prior models [1,10,35] and environmental data from the Hong Kong Observatory (HKO). Chloride content deposition predictions stem from boundary values by chloride ion test in the GBA area and models from relevant studies [48]. For temperature evaluation, the time-varying temperature $T_{\text{pred}}(t)$ (Eq.(7)) comprises an average baseline T_{base} , a sinusoidal variation T_{ana} (Eq.(8)), an increasing trend $T_{\text{inc}}(EC, t)$ (EC is the characteristic value of environmental temperature), and temperature noise T_{λ} following Gaussian distribution $N(0, \sigma_{T_{\lambda}})$.

$$T_{\text{pred}}(t) = T_{\text{base}} + T_{\text{ana}}(t) + T_{\text{inc}}(EC, t) + T_{\lambda} \quad (7)$$

$$T_{\text{ana}}(t) = \sum_{i=1}^{n_{\text{temp}}} a_{1,i}^T \sin \left[a_{2,i}^T \cdot (t + 1885) + a_{3,i}^T \right] \quad (8)$$

$$T_{\text{inc}}(EC, t) = b_1^T(EC) \cdot (t - t_{\text{ref}})^{b_2^T(EC)} \quad (9)$$

where t (year) is the time elapsed since 1885; n_{temp} is the term number of T_{ana} ; $b_{1,i}^T$, $b_{2,i}^T$ and $b_{3,i}^T$ ($i=1, \dots, n_{\text{temp}}$) are the coefficients of T_{ana} ; t_{ref} is the reference year (85 year); and $b_1^T(EC)$ and $b_2^T(EC)$ are power function parameters of $T_{\text{inc}}(EC, t)$ (as described in Eqs.(10) and (11)), relating to the temperature rising tendency from 1970 to the investigated year, considering the characteristic EC which follows a bimodal distribution of $0.5N(1.8, 0.2) + 0.5N(3, 0.13)$ [49].

$$b_1^T(EC) = 5.04 \times 10^{-3} EC^2 - 3.57 \times 10^{-2} EC + 6.49 \times 10^{-2} \quad (10)$$

$$b_2^T(EC) = 3.59 \times 10^{-1} EC + 3.33 \times 10^{-1} \quad (11)$$

The fitting results of Eq.(8) and their 95% confidence interval are displayed in Fig. 5a, while the fitted coefficients of T_{ana} and $\sigma_{T_{\lambda}}$ are summarized in Table 5. Fig. 5b portrays the predicted annual temperature variation based on typical EC s (1.1 and 3.5°C), offering insights into the expected temperature trends in the future.

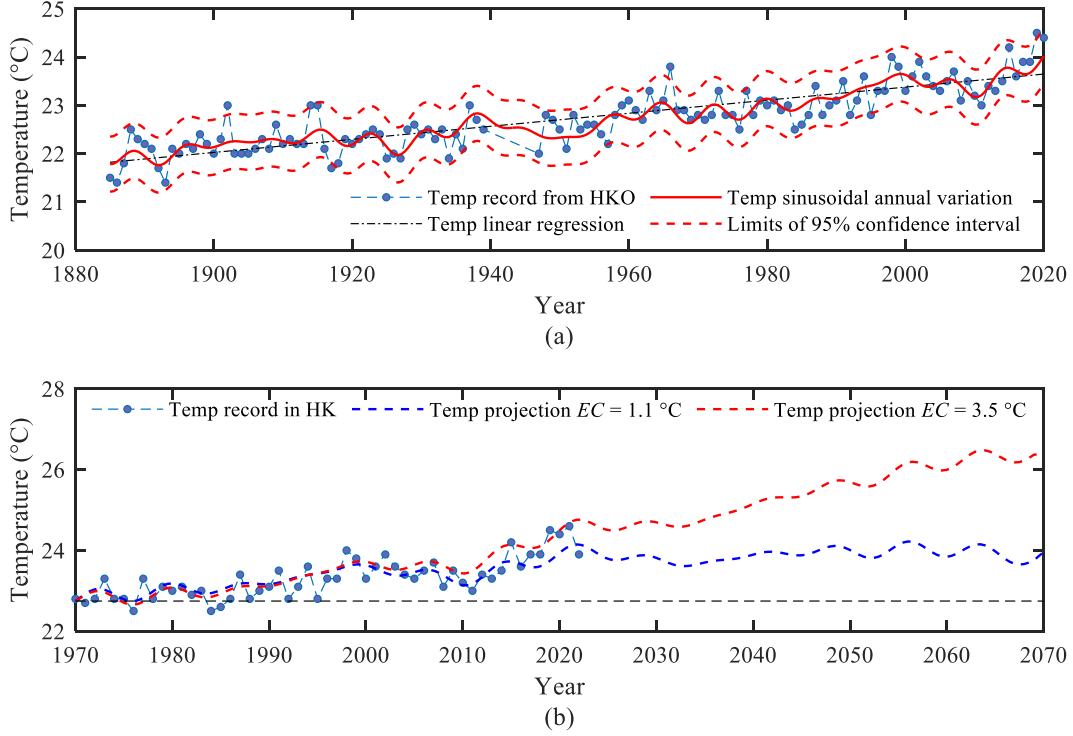


Fig. 5 Temperature regression model in GBA: (a) comparisons of recorded temperature and model evaluation; and (b) comparisons of recorded temperature and temperature projections subject to different EC s

Table 5 Coefficient values of annual variation and distribution parameters of T_λ for temperature

Coefficients	$a^{T_{1,1}}$	$a^{T_{2,1}}$	$a^{T_{3,1}}$	$a^{T_{1,2}}$	$a^{T_{2,2}}$	$a^{T_{3,2}}$	$a^{T_{1,3}}$	$a^{T_{2,3}}$	$a^{T_{3,3}}$
Values	0.1557	0.04286	8.692	0.1126	0.3072	27.97	0.1421	0.2193	22.83
Coefficients	$a^{T_{1,4}}$	$a^{T_{2,4}}$	$a^{T_{3,4}}$	$a^{T_{1,5}}$	$a^{T_{2,5}}$	$a^{T_{3,5}}$	n_{temp}	σ_{T_λ}	
Values	0.1025	0.8969	42.27	0.09829	0.755	45.41	5	0.29	

For RH assessment, h_{pred} (Eq.(12)) includes Fourier series h_{ana} (Eq.(13)) and humidity noise h_λ . The distribution parameter of h_λ is fitted based on the residual error of Eq. (13). The fitting results of Eq.(13) and their corresponding 95% confidence interval are displayed in Fig. 6, while the coefficients of h_{ana} and σ_{h_λ} are summarized in Table 6.

$$h_{pred}(t) = h_{ana}(t) + h_\lambda \quad (12)$$

$$h_{ana}(t) = 100 \cdot h_c + \sum_{i=1}^{n_h} a_{1,i}^h \cos(i \cdot \omega^h \cdot (t+1961)) + \sum_{i=1}^{n_h} a_{2,i}^h \sin(i \cdot \omega^h \cdot (t+1961)) \quad (13)$$

where t (year) is the time from 1961; n_h is the term number of h_{ana} ; h_c , $a_{1,i}^h$, $a_{2,i}^h$ and ω^h ($i=1, \dots, n_h$) are the coefficients of h_{ana} .

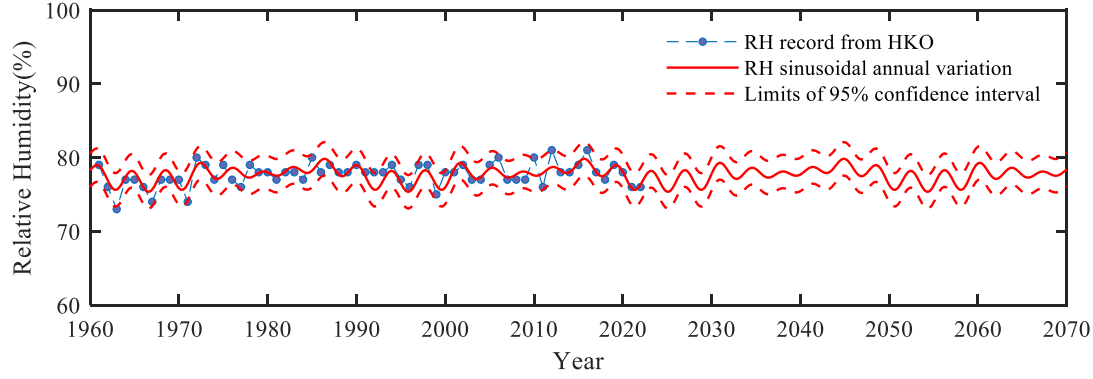


Fig. 6 Comparisons of recorded RH from HKO and model evaluation

Table 6 Coefficient values of annual variation and distribution parameters for RH

Coefficients	h_c	$a^{h_{1,1}}$	$a^{h_{2,1}}$	$a^{h_{1,2}}$	$a^{h_{2,2}}$	$a^{h_{1,3}}$	$a^{h_{2,3}}$	$a^{h_{1,4}}$	$a^{h_{2,4}}$	σ_{hl}
Values	0.7773	0.2098	-0.7099	0.4716	-0.2965	-0.06217	-0.1261	0.1188	-0.1018	1.1566
Coefficients	ω	$a^{h_{1,5}}$	$a^{h_{2,5}}$	$a^{h_{1,6}}$	$a^{h_{2,6}}$	$a^{h_{1,7}}$	$a^{h_{2,7}}$	$a^{h_{1,8}}$	$a^{h_{2,8}}$	
Values	0.2149	-0.02508	0.06674	-0.01068	-0.1048	0.00343	0.5987	-0.9325	0.08894	

Additionally, it is challenging to establish a physically driven and universal chloride deposition prediction model. Also, the surface chloride content data obtained from the in-situ study is limited [50], making it difficult to employ complex models for chloride deposition prediction. Therefore, a power function segmentation model, represented as Eq. (14) and derived by fitting the measured data [36], is utilized for the surface chloride content

$$C_{sa} = \begin{cases} C_{sa,1} \cdot t^{n_{sa}}, & t < 20 \text{ years} \\ C_{sa,20}, & t \geq 20 \text{ years} \end{cases} \quad (14)$$

where t (year) is the time from the construction done; $C_{sa,1}$ stands for the surface chloride content after 1 year of exposure (0.53%wt cement [50]); n_{sa} is an empirical coefficient; and $C_{sa,20}$ is the surface chloride content after 20 years of exposure (1.986%wt cement [50]).

4.3 Durability estimation model

4.3.1 Chloride ingress

Prior research demonstrated that in rectangular cross-section components such as beams and columns, the chloride ion content on the surfaces of corner steel bars ($C_{Cl,cor}$) surpasses that of middle steel bars ($C_{Cl,mid}$), resulting in the earlier de-passivation of corner bars [51]. To precisely evaluate $C_{Cl,cor}$ and $C_{Cl,mid}$, a validated 2D predictive model for chloride transport in ordinary Portland cement concrete is employed (Eq.(15)) [10].

$$\frac{\partial C_{fc}}{\partial t} = \text{div}(D_c^* \nabla C_{fc}) + \text{div}(C_{fc} D_h^* \nabla h_{RH}) \quad (15)$$

where C_{fc} (kg/m³ of pore solution) represents the content of free chloride ions; h_{RH} is the relative humidity (RH) in the pore solution; and D_c^* and D_h^* signify the apparent diffusion coefficients of chloride ions and humidity, respectively [10]. Additionally, moisture transport and heat transfer can be included as follows:

$$\frac{\partial w_e}{\partial h} \frac{\partial h_{RH}}{\partial t} = \text{div}(D_h \cdot \nabla h_{RH}) \quad (16)$$

$$\rho_c c_q \frac{\partial T}{\partial t} = \text{div}(\lambda \cdot \nabla T) \quad (17)$$

where D_h stands for the diffusion coefficient of RH (m^2/s), estimated through Saetta et al.'s model [52]; and ρ_c , c_q ($10^3 \text{ J}\cdot\text{kg}^{-1}\text{K}^{-1}$ [53]), and λ ($2.5 \text{ W}\cdot\text{m}^{-1}\text{K}^{-1}$ [51]) denote the density, heat capacity, and thermal conductivity of concrete, respectively.

Before solving Eqs. (15)-(17), it is imperative to establish the boundary conditions (as elaborated in Section 4.1) and specify the material properties of concrete. Due to the seasonal variation of environmental parameters, despite the investigated service life being 50 years, the time step for the mass transport investigation is set at half-day. The computation process for Eqs. (15)-(17) is further divided into three fundamental steps [10,54]:

- (1) Solving the heat transfer equation, Eq. (17);
- (2) Solving the moisture diffusion equation Eq.(16), based on the solution derived from the heat transfer equation; and
- (3) Solving the chloride transport equation Eq.(15), based on the solutions derived from the heat transfer and moisture transfer equations.

Given the pronounced non-linearity within Eqs. (15)-(17), FDM is utilized for numerical solutions. Additionally, for two-dimensional transport, the alternating-direction implicit (ADI) FDM is implemented [10], leveraging the ADI scheme's unconditional stability and high accuracy attributes [55]. To verify the accuracy of the chloride transport model, a study by Pang and Li[50] is introduced, involving a chloride ingress survey on pre-2000 RC high piling wharves in Bao'an District of Shenzhen, and Hong Kong. Table 7 presents a comprehensive overview of crucial details for the investigated structures, encompassing locations, construction and investigation years, concrete grades, and water-cement ratios. The reference diffusion coefficient of chloride, denoted as $D_{c,\text{ref}}$ (m^2/s), displays nonlinearity and randomness influenced by factors such as the water-to-cement ratio (w/c) and admixture content. Consequently, accurately assessing $D_{c,\text{ref}}$ poses a considerable challenge. In alignment with existing relevant studies [52,56], the values for $D_{c,\text{ref}}$ under Case 1 to 5 are adopted as 4×10^{-11} , 2×10^{-11} , 1.2×10^{-11} , 6×10^{-11} , and 4×10^{-11} , respectively.

Table 7 Characteristics of investigated structures [50]

No	Location	Construction year	Investigation year	Concrete grade	w/c
Case 1	SZ	1994	2008	C30	0.45
Case 2	SZ	1988	2008	C25	0.45
Case 3	SZ	1987	2007	C30	0.4
Case 4	HK	1984	2007	C25	0.65
Case 5	HK	1984	2008	C25	0.5

Note: SZ and HK denote Shenzhen and Hong Kong, respectively.

Applying the environmental models (Section 4.1), the boundary conditions for temperature, moisture, and surface chloride content were established. Using FDM and data in Table 7, Eqs.

Eqs. (15)-(17) were solved. Fig. 7 illustrates a comparison between computational results and experimental data. As displayed, the numerical curves closely align with the experimental curves for most cases outlined in Table 7. The coefficient of determination (R^2) for all cases surpasses 0.8, signifying the accuracy of the chloride transport model in capturing the trends of chloride ingress over time in RC structures along the Greater Bay Area (GBA) coastline. This accuracy is maintained consistently across various factors, including location, construction year, and water-to-cement ratio.

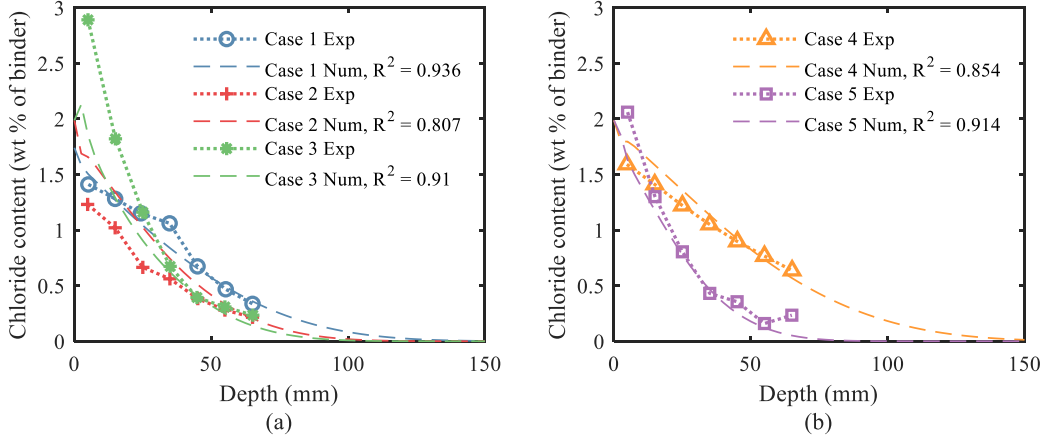


Fig. 7 Comparisons of experimental and calculated chloride profiles under different locations: (a) Shenzhen; and (b) Hong Kong (R^2 denotes the coefficient of determination)

4.3.2 Corrosion propagation damage

When the chloride content on the surfaces of steel bars ($C_{Cl,cor}$ and $C_{Cl,mid}$) surpasses the critical chloride content C_{cr} , corrosion initiation occurs, requiring quantification of corrosion extent. Herein, the corrosion rate i_{corr} ($\mu A/cm^2$) is determined through an empirical model [37]:

$$\ln(1.08i_{corr}) = 7.89 + 0.7771\ln(1.69C_{Cl}) - 3006/T - 0.000116R_c + 2.24t^{-0.215} + \mathcal{G} \quad (18)$$

where T (K) represents the temperature within the concrete; R_c (Ohms) is the resistance of the cover concrete; and \mathcal{G} is a Gaussian random variable that represents the model deviation, following $N(0, 0.3312)$. Following Faraday's law, the average radius loss (Δr) and the minimum residual cross-sectional area (A_{min}) of steel bars can be calculated using Eqs. (19) and (20) [12].

$$\Delta r = \int 0.0116i_{corr} dt \quad (19)$$

$$A_{min} = 0.25\pi d_0^2 (1 - \eta_{max}) = 0.25\pi d_0^2 (1 - \eta_{ave}) / R_0 = 0.25\pi (d_0 - 2 \cdot \Delta r)^2 / R_0 \quad (20)$$

where d_0 is the initial diameter of the steel bar; η_{ave} and η_{max} denote the average and maximum corrosion degrees of corroded steel bars, respectively, and R_0 is the corrosion non-uniformity factor of the average to minimum cross-sectional area. The distribution parameters (μ and σ) of the factor R are computed by Eqs. (21) and (22) [7].

$$\mu = 3.35\eta_{ave} \cdot \exp(-0.236i_{corr}) + 0.12\eta_{ave} + \sigma \cdot \ln(l_{bar} / 50) + 1.01 \quad (21)$$

$$\sigma = 0.3371\eta_{ave} + 0.0006 \quad (22)$$

where l_{bar} is the analysis length of the investigated steel bar. Regarding the loss of cross-sectional area $\Delta A_s(t)$ over time, the corrosion-induced crack width ω (mm) is assessed using an empirical model [38]:

$$\omega(t) = 0.0575 \cdot [\Delta A_s(t) - \Delta A_{s0}], \Delta A_{s0} = \pi d_0^2 \left\{ 1 - \left[1 - 2/d_0 (7.53 + 9.32c_t/d_0) 10^{-3} \right]^2 \right\} \quad (23)$$

where ΔA_{s0} is the reduction of the cross-sectional area when concrete cracks, and c_t (mm) is the concrete cover. Considering the impact of corrosion-induced cracks on the concrete durability, the diffusion coefficients of chloride (D_c^ω) and humidity (D_h^ω) for cracked concrete are evaluated using Eqs.(24) [57] and (25) [39], respectively.

$$D_c^\omega = f_{\omega 1}(\omega) \cdot D_c^*(t), f_{\omega 1}(\omega) = 31.61\omega^2 + 4.73\omega + 1, \omega \geq 0.1 \text{ mm} \quad (24)$$

$$D_h^\omega = f_{\omega 2}(\omega) \cdot D_h^*(t), f_h(\omega) = 1 + k_h \cdot \omega^3 / s_h \quad (25)$$

where k_h and s_h are environmental factors (10^5 mm^{-2} [39]) and mean crack spacing [39], respectively.

4.4 Mechanical behavior estimation model

This study utilizes a semi-analytical section model to assess the flexural capacity of corroded RC beams, considering bond strength reduction due to corrosion [1]. The effective bond force $F_{t\eta}$ diminishes, leading to varying strains between tension bar ε_s and surrounding concrete ε_{cs} , quantified by compatibility coefficient Ω (Eq.(26)) [32].

$$\Omega = \varepsilon_s / \varepsilon_{cs} \quad (26)$$

A simplified expression for Ω is derived via regression analysis (Eq. (27)), encompassing corrosion degrees, loading configurations, span-height ratios, etc. [32]

$$\Omega = 0.09 + 0.9l_p/l_0 + 8(1 - l_p/l_0) \exp(0.09l_p/h_0 - 30\eta_{\max} - 0.81) \leq 1.0 \ \& \ \geq 0.15 \quad (27)$$

where l_0 and h_0 denote the effective span and height of the beam, and l_p is the distance between two-point loads for a four-point loaded beam. The validation of Eq. (27) can be found in previous studies [1,32]. When the tension force F_s of the corroded steel bar falls surpasses $F_{t\eta}$ (Eq.(28)), ε_s becomes ε_{cs} multiplied by Ω , and the flexural behavior can still be evaluated using a nonlinear sectional analysis grounded on the assumption of the plane section [40,58].

$$F_{t\eta} = \pi d_{t0} \cdot l_d \cdot \tau_{bu0} \cdot R(\eta_{\max}) \quad (28)$$

where d_{t0} is the initial diameter of the tension bar; l_d is the length of the effective bond region (evaluated by ACI 318 [59]); τ_{bu0} is the average bond stress for uncorroded bars [40,60]; and $R(\eta_s)$ is the normalized bond strength evaluation model [40]. Details of Eq.(28) refer to [32,40].

Besides, a trilinear constitutive model for corroded steel bars is adopted [7,61]. Elastic modulus (E_{s0}), actual yield strength (f_{y0}), and ultimate strength (f_{u0}) remain constant, whereas the hardening strain ε_{sh} and ultimate strain ε_{su} decrease with corrosion degree [33]:

$$\varepsilon_{sh} = \begin{cases} \frac{f_{y0}}{E_{s0}} + \left(\varepsilon_{sh0} - \frac{f_{y0}}{E_{s0}} \right) \left(1 - \frac{\eta_{\max}}{\eta_{cr}} \right), \eta_{\max} \leq \eta_{cr} \\ \varepsilon_{sy} = \frac{f_{yc}}{E_{s0}}, \eta_{\max} > \eta_{cr} \end{cases} \quad (29)$$

$$\varepsilon_{su} = \exp(-\beta_{\delta} \eta_{\max}) \varepsilon_{su0}, \quad (30)$$

where η_{cr} represents the critical corrosion degree, ranging from 20% to 30% [61]; ε_{sh0} and ε_{su0} denote the hardened strain and ultimate strain of non-corroded steel bars; and β_{δ} equals 2.093 and 2.501 for salt spray-induced corrosion and natural corrosion, respectively [34].

Regarding the nonlinear attributes of concrete, a nonlinear constitutive model is applied, in which the principal tension stress σ_{c1} and compressive stress σ_{c2} are as follows:

$$\sigma_{c1} = E_c \cdot \varepsilon_1 \cdot H(\varepsilon_{cr} - \varepsilon_1) \quad (31)$$

$$\sigma_{c2} = f_c \left[2(\varepsilon_2/\varepsilon_0) - (\varepsilon_2/\varepsilon_0)^2 \right] \quad (32)$$

where ε_1 and ε_2 stand for the principal tensile and compressive strains, respectively, and ε_{cr} and ε_0 represent the tensile strain of concrete corresponding to the tensile strength f_t and the compressive strain corresponding to the peak compressive stress f_c , respectively.

Considering the non-rectangular cross-section of the hollow beam, the flexural capacity analysis is conducted using the cross-section layering method based on the bisection method-based iterative algorithm [62]. Such a computational process yields the non-linear moment-curvature relationship and residual flexural capacity (M_{res}) at each time point [32].

5. Establishment of a performance prediction model

5.1 Information for model establishment

This study employs the LightGBM model to construct surrogate models predicting the life-cycle performance of RC hollow beams. To address input variable uncertainties (Table 1), LHS is utilized to generate 1,000 samples [63], forming a dataset for training the surrogate model for RC hollow beams of 6m, 8m, and 10m spans (Fig. 1, step 1). Due to the double-looping computation for 50 years of service for each sample, the dataset size becomes the product of the number of samples and the number of time steps. Before training, the dataset is randomly split into 70% for training and 30% for testing (Fig. 1, step 2).

The training dataset utilizes Bayesian optimization and 10-fold cross-validation (10-fold CV) to determine optimal surrogate models. Bayesian optimization utilizes Gaussian process regression for hyperparameter modeling, with the acquisition function sampling hyperparameters. The acquisition function is used to balance exploration and exploitation. It guides the search for the next point to evaluate in the objective function. These functions use the Gaussian process model's predictions to suggest where the optimization process should focus next. The Bayesian optimization process is iterative until a satisfactory solution is found or a predefined stopping criterion is met.

10-fold CV divides the dataset into ten groups, using nine for training and one for validation. The optimal LightGBM model is determined by averaging evaluation scores' means, with the

coefficient of determination (R^2) serving as the evaluation metric. R^2 , ranging from 0 to 1, gauges similarity between predicted and actual values. Utilizing precise subject-specific vocabulary is crucial, and a high R^2 -value characterizes a precise surrogate model.

The LightGBM surrogate model learns patterns and relationships between features and target performance metrics of RC hollow beams from training data. Once developed and verified, it accurately forecasts endurance and mechanical reactions across different life cycle stages using input parameters from an untrained testing dataset. By entering relevant feature values representing various periods, the model ensures precision. Employing Bayesian hyperparameter optimization and a 10-fold CV approach, the study determines optimal hyperparameters for each LightGBM surrogate model predicting the life-cycle performance of RC hollow beams. These hyperparameters include learning rates, the number of estimators, maximum depth, minimum sum of instance weight, minimum number of data needed in a child, subsample ratio of the training instance, subsample ratio of columns when constructing each tree, and the L1 and L2 regularization terms on weights.

5.2 Model prediction performance

Table 8 displays the prediction performance of each LightGBM surrogate model on the untrained test dataset. All models achieve R^2 values surpassing 99.9%, emphasizing the remarkable accuracy in predicting the life-cycle performance of RC hollow beams. Moreover, utilizing the trained LightGBM surrogate model for life-cycle performance forecasting requires only 1 second, a notable improvement of 1000 times compared to conventional numerical simulation methods.

Table 8 Evaluation metrics for each surrogate model on the untrained test dataset

R^2	6m span	8m span	10m span
C_{fc}	99.9850%	99.9842%	99.9781%
C_{tc}	99.9545%	99.9556%	99.9398%
$\eta_{ave,ten}$	99.9901%	99.9771%	99.9869%
$\eta_{ave,com}$	99.9912%	99.9818%	99.9897%
$\eta_{max,ten}$	99.9307%	99.9338%	99.9291%
$\eta_{max,com}$	99.9382%	99.9360%	99.9335%
M_{res}	99.9349%	99.9349%	99.9349%

Fig. 8 and Fig. 9 depict the detailed accuracy of life-cycle performance predictions. In Fig. 8, the alignment of most points with the diagonal line illustrates strong concurrence between model predictions and actual values for an RC hollow beam with a 10m span. Slight deviations from the diagonal are deemed acceptable in the context of ML predictions.

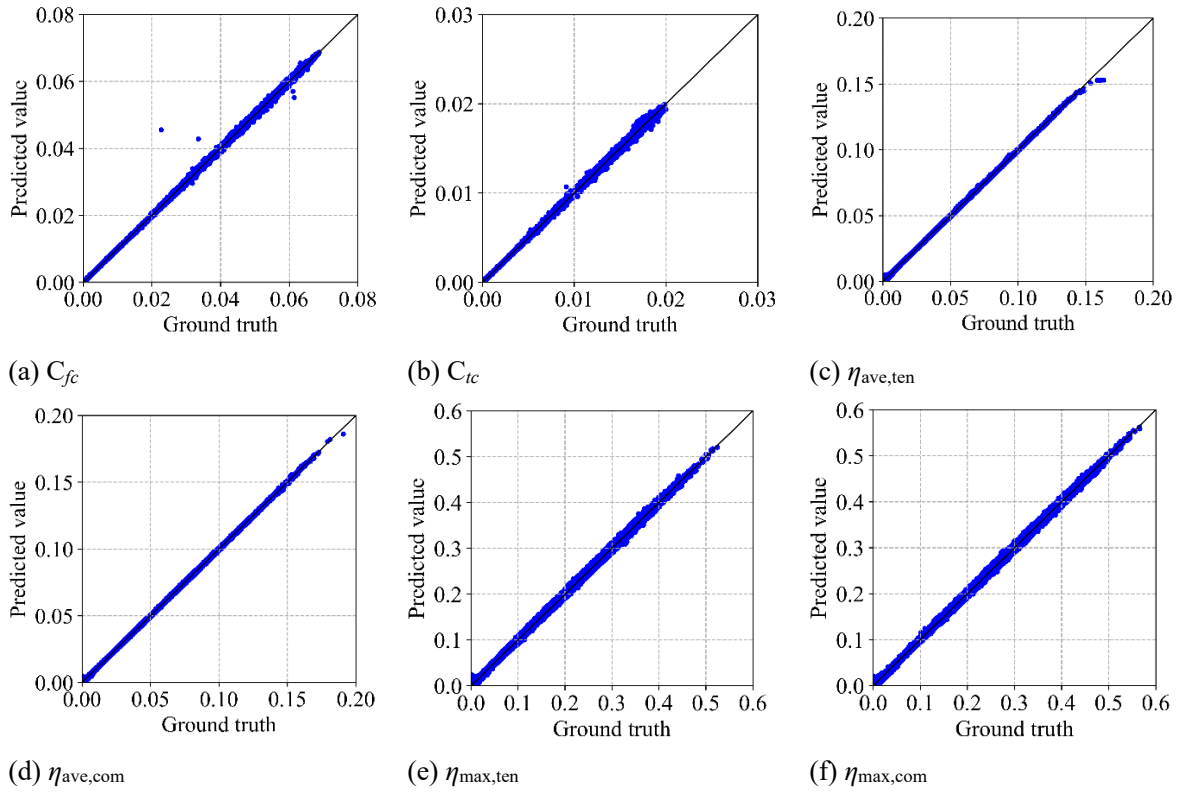


Fig. 8 Relation between tested (Ground truth) and predicted value in span of 10m

Moving to Fig. 9, the relation between tested and predicted residual bending capacity for spans of 6m, 8m, and 10m is shown. The first row represents the entire test dataset, while the second row displays a sample, juxtaposing predicted life-cycle values with corresponding ground truth. In Fig. 9d to f, the close alignment of the red dashed line with the black solid line reaffirms the high accuracy of the built model in residual bending capacity prediction over the service life. Furthermore, in Fig. 9d to f, the plots of residual bending capacity versus time show fluctuations in the declining rate after corrosion initiation. Initially, a rapid decline occurs after corrosion initiation, followed by a gradual deceleration. As time goes by, concrete cracking increases the declining rate, leading to intermittent sharp declines [13].

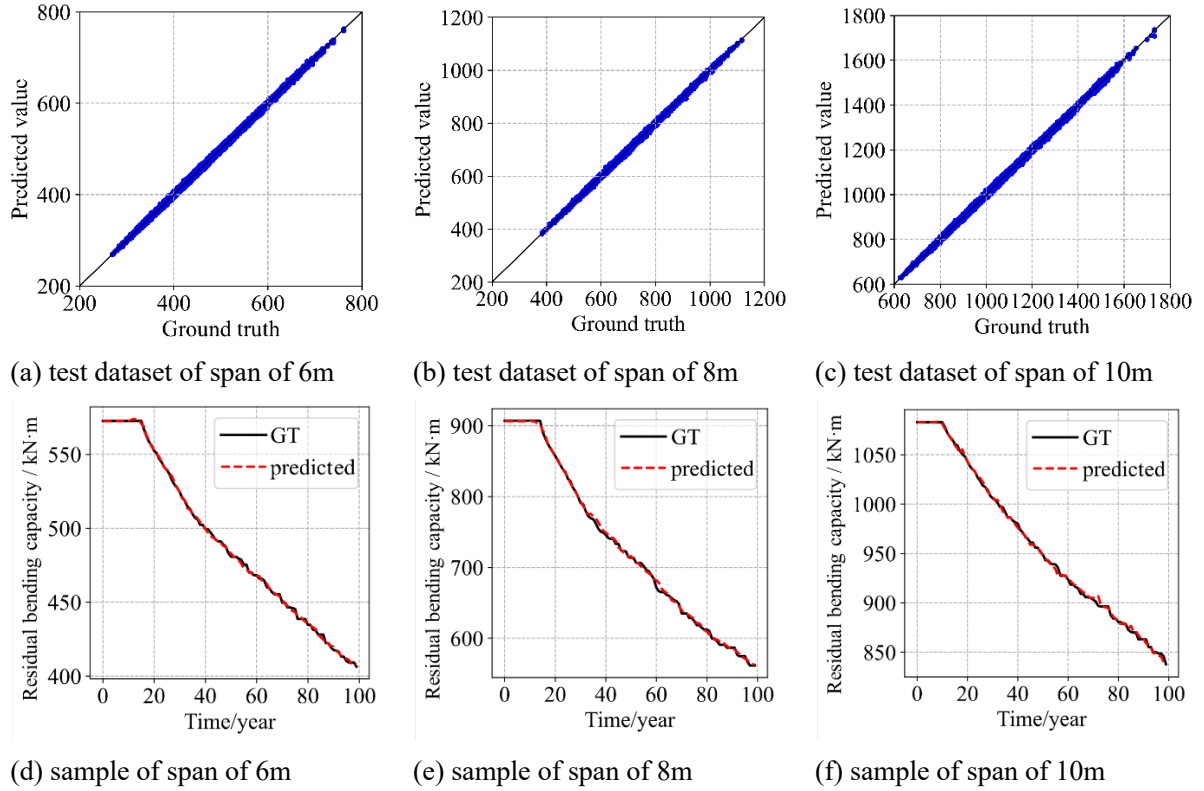


Fig. 9 Relation between tested (Ground truth, GT) and predicted residual bending capacity

5.3 Performance comparison with different surrogate models

This study compares the predictive capabilities of the LightGBM model with three EL models (Random Forest - RF, Gradient Boosting Decision Tree - GBDT, XGBoost) and one deep learning model (Residual Network - ResNet). RF belongs to the family of bagging ensemble algorithms, and it builds multiple decision trees during training. Unlike RF, GBDT builds multiple independent trees in parallel. ResNet introduces the concept of residual learning in the deep neural networks, where each layer learns the residual with respect to the previous layer's output [64]. All models are trained and tested on the same datasets, and Bayesian optimization with a 10-fold CV technique determines optimal hyperparameters.

In Fig. 10, the prediction accuracy is measured with R^2 . Meanwhile, training efficiency is measured with training time, which is then standardized relative to the training time of the LightGBM model. It can be seen that despite the high prediction accuracy observed in all five models, LightGBM outperforms XGBoost and ResNet models with the highest R^2 value at 99.9581%. Regarding training efficiency, the LightGBM model outperforms other models by at least 1 time, and with larger datasets, the computational time saved by this model becomes even more substantial. Overall, the LightGBM model stands out among these models, offering both speed and accuracy in predicting the life-cycle performance of RC structures.

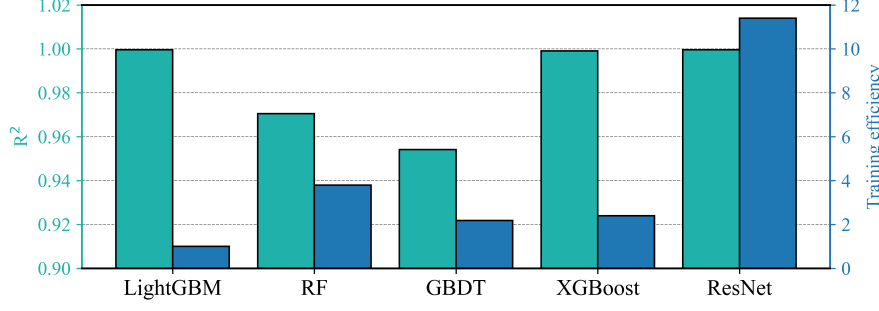


Fig. 10 Comparison of life-cycle performance prediction accuracy with different surrogate model

Efficiency evaluation is crucial for comparing surrogate models, focusing on training times in this study. Compared to the LightGBM baseline, the training times for DT, SVM, RF, GBDT, and GPR models are 0.321, 0.339, 2.658, 2.196, and 5.326 times that of the proposed model, respectively. Single weak learners (DT and SVM) exhibit quick training but lower prediction accuracy than EL methods. LightGBM emerges as the most efficient among EL methods, excelling in both training efficiency and prediction accuracy. In summary, LightGBM demonstrates robust predictive capabilities, surpassing other EL models in terms of accuracy and efficiency.

6. Interpretation of performance predictions

The SHAP analysis of the LightGBM surrogate model reveals the significance of individual physical and environmental parameters in determining the overall durability and mechanical measures of RC hollow beams. This analysis provides a comprehensive understanding of how the model makes predictions, offering both a global perspective and insights into the importance of specific features for each prediction. It enhances our understanding of the model's decision-making process regarding durability and mechanical performance.

6.1 Global interpretation of feature effects

The global interpretation of SHAP involves understanding the general behavior of the trained LightGBM surrogate model and the influence of various physical and environmental features on durability and mechanical predictions. SHAP values, representing average feature contributions across all data points, are crucial for this interpretation. The SHAP summary plot provides insights into feature importance rankings, aiding in a deeper understanding of the overall behavior of the model and identifying significant patterns and relationships among features.

In Fig. 11, SHAP summary plots for selected measures focus on 10m span RC hollow beams, visually depicting the impact of physical and environmental features on predictions. Concrete resistivity (R_c) emerges as crucial for $\eta_{ave,ten}$ and $\eta_{ave,com}$, ranking second for C_{tc} and M_{res} . Reference chloride diffusion coefficient ($D_{c,ref}$) and critical chloride content (c_{cr}) are prominent for $\eta_{ave,ten}$ and $\eta_{ave,com}$. Corrosion non-uniformity (R_0) holds the second-most important position for $\eta_{ave,com}$. EC characteristic value influences $\eta_{ave,ten}$, $\eta_{ave,com}$, and C_{tc} predictions. The horizontal position of each data point in Fig. 11 indicates whether feature values increase or decrease predictions. For instance, a higher R_c leads to lower predictions for $\eta_{ave,ten}$, $\eta_{ave,com}$, and C_{tc} , while higher $D_{c,ref}$ results in higher predictions. Notably, the influence range of R_0 on $\eta_{max,ten}$

prediction exhibits distinct effects in the positive and negative regions. A higher R_0 value causes a larger increase in $\eta_{\max,ten}$, while a lower R_0 value results in a more pronounced decrease in $\eta_{\max,ten}$. Similarly, the variation in c_{cr} also shows the opposite effect on the prediction of C_{tc} . Furthermore, across the entire dataset, f_{y0} appears to have a substantial influence on M_{res} compared to other input physical and environmental parameters. The variations in ranking for the prediction of M_{res} throughout the service life warrant further investigation.

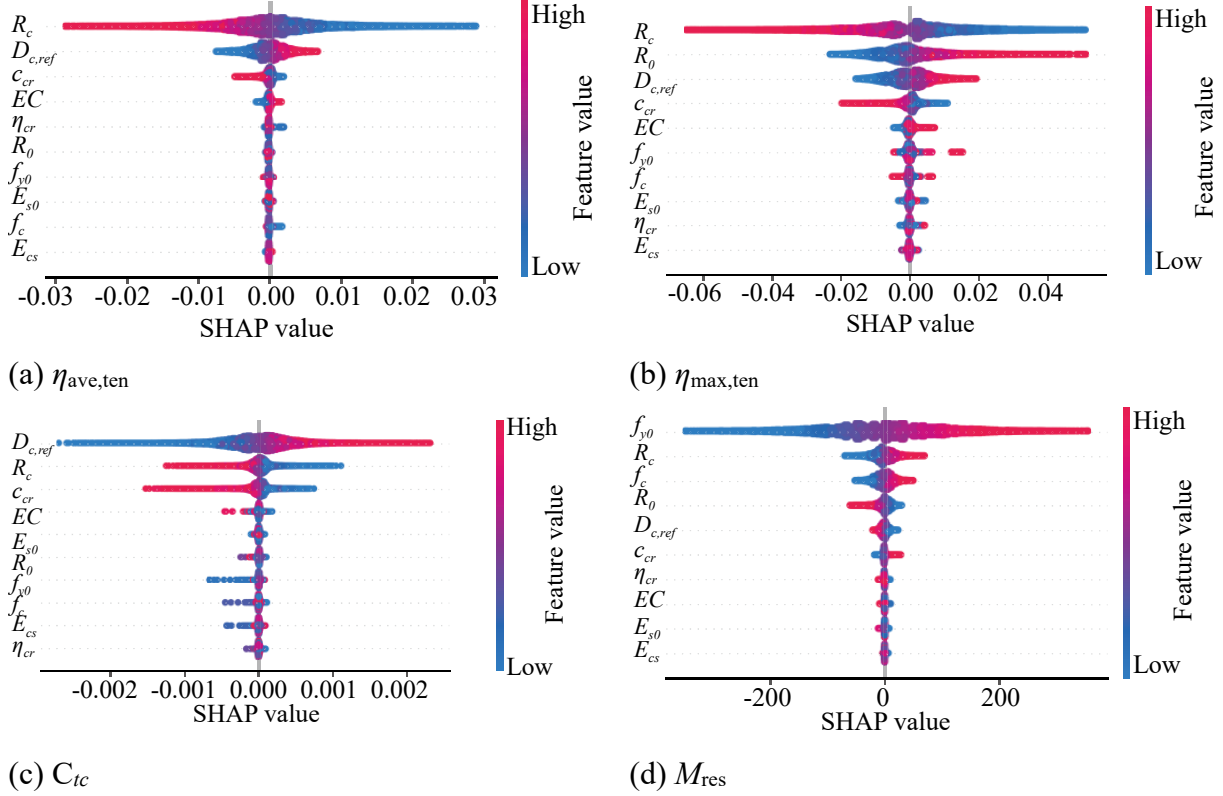
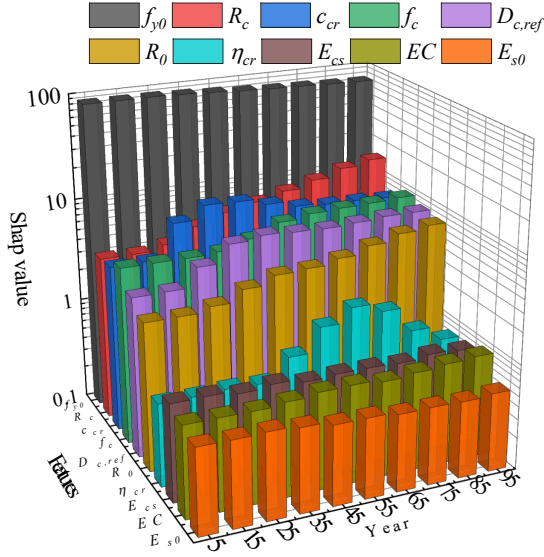
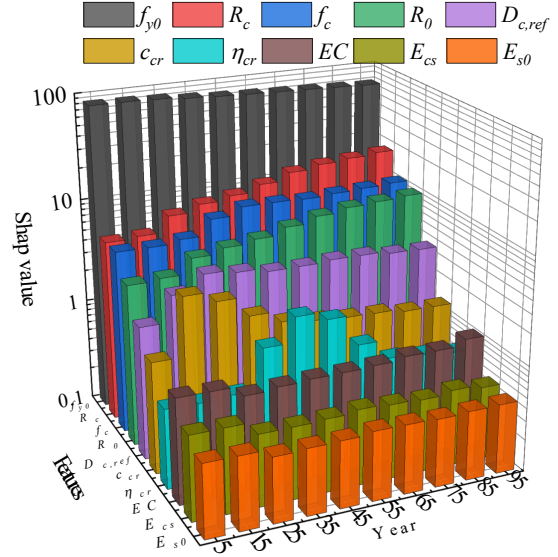


Fig. 11 Global interpretations of LightGBM model by SHAP values in span of 10m

Fig. 12 displays feature importance and SHAP value variations for predicting M_{res} in a 10m span RC hollow beam, considering both 1-D and 2-D chloride ion transport. These results illuminate changing significance and influence of input features on M_{res} predictions over the service life. f_{y0} remains dominant, while c_{cr} , R_c , f_c , and $D_{c,ref}$ gain importance over time. In 1D chloride ion transport, c_{cr} ranks second from 25th to 55th year, indicating increasing importance. Rankings for R_c , c_{cr} , f_c , and $D_{c,ref}$ vary with time, underlining their growing significance in determining M_{res} . In 2D chloride transport, the effects of R_c , c_{cr} , and R_0 on M_{res} predictions become more pronounced over time. These findings underscore the dynamic nature of the prediction process of the LightGBM model in the life cycle analysis of M_{res} for RC hollow beams. Understanding these changes is crucial for identifying factors influencing mechanical resistance at different life cycle stages, guiding decisions and optimization strategies for enhanced durability and performance.



(a) 1-D chloride transport



(b) 2-D chloride transport

Fig. 12 Feature importance ranking variations on residual bending moment prediction during life-cycle in span of 10m

6.2 Analysis of significant feature dependencies

The individual interpretation of SHAP offers detailed insights into how each physical and environmental feature contributes to durability and mechanical predictions for specific instances. It assesses feature impact relative to a baseline or reference prediction, indicating whether a feature positively or negatively influences that specific prediction.

To visualize individual explanations, the SHAP dependence plot is employed. In a SHAP dependence plot, the horizontal axis represents feature values, the vertical axis corresponds to associated SHAP values, and data point color indicates interactions with another feature. Positive SHAP values are in red, while negative values are in blue. Besides, vertical dispersion of the data points reflects the magnitude of interaction effects between features.

Fig. 13 presents feature dependence plots for M_{res} in a 10m span. As shown, f_{y0} , R_c , and f_c positively impact M_{res} , while R_0 has a negative impact. In Fig. 13b to d, considering the same feature values of R_0 , R_c , and f_c , red points move farther from zero over time, indicating their increasing impact on M_{res} predictions. Conversely, in Fig. 13a and e, the impact of f_{y0} and c_{cr} on M_{res} decreases with time. In Fig. 13a, the narrow vertical dispersion suggests time has a limited influence on the impact of f_{y0} on M_{res} , while other features exhibit larger dispersion, indicating more significant changes in their impact over time. These insights offer a detailed understanding of how individual features affect M_{res} predictions over the service life, guiding targeted strategies for optimizing structural durability and performance.

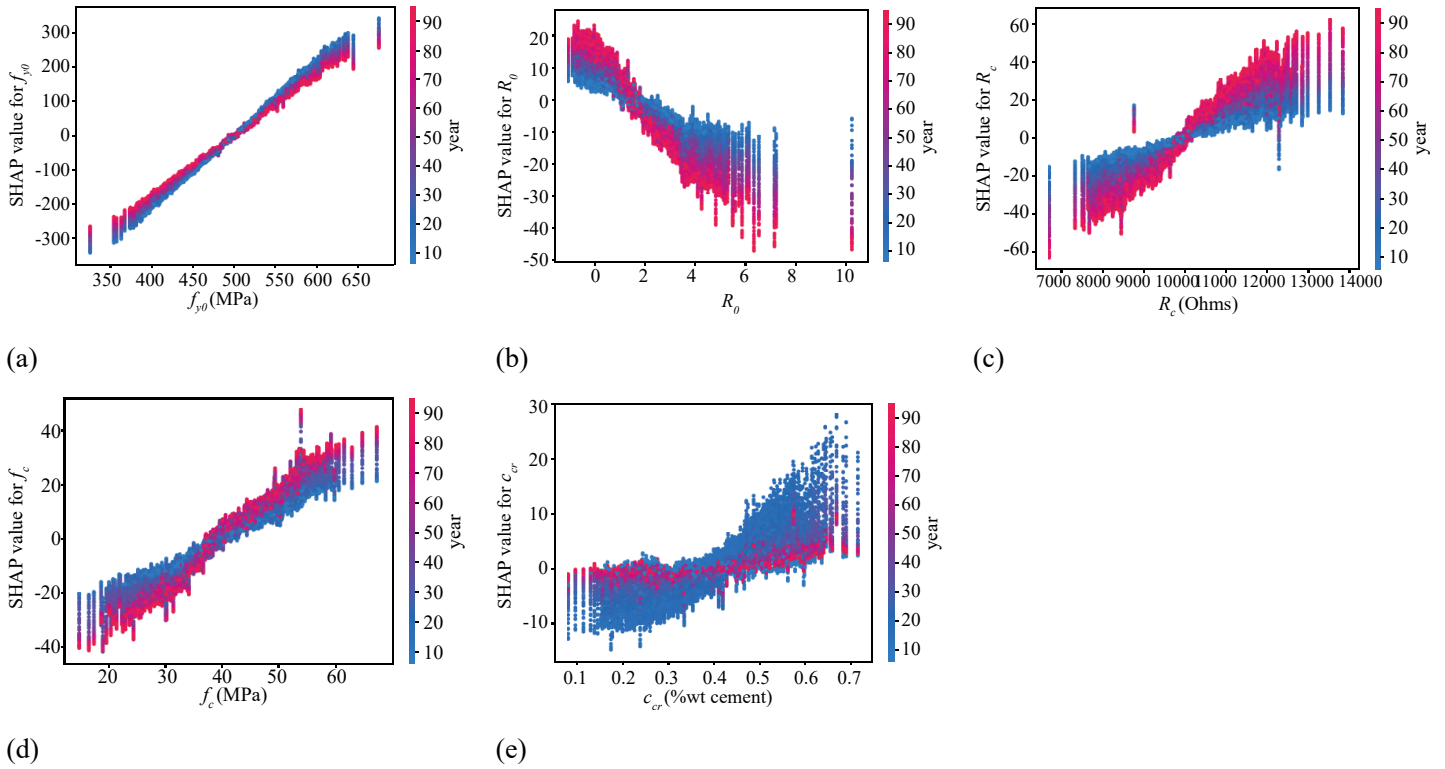


Fig. 13 Feature dependence plots for M_{res} in span of 10m

6.3 Impact of climate change on residual bending capacity

The trained LightGBM model will further assess the impact of climate change on the residual bending capacity at the end of service life. Considering the bimodal distribution of the characteristic value of EC , two climate change scenarios will be examined: small EC (1~1.8°C) and large EC (3~3.5°C). SHAP dependence plots in Fig. 14 reveal the relationship between critical physical and environmental parameters and bending capacity, where solid curves depict general trends, offering insights into the effects of the parameters under global warming.

Unlike the results in Fig. 13, the effects of c_{cr} , EC , E_{cs} , and E_{s0} on M_{res} reflect a stronger nonlinearity and discreteness. Also, comparing the feature dependence plot on the left and right sides of Fig. 14, it is seen that the effects of c_{cr} , EC , E_{cs} , and E_{s0} on M_{res} are also different under small (blue results) and large (red results) EC . For instance, in Fig. 14a, it can be noticed that under the small EC , the SHAP value of c_{cr} sharply decreases with c_{cr} , dropping to around 0.45 and then increasing. Conversely, under the large EC , the SHAP value of c_{cr} essentially decreases with c_{cr} , but the reduction is less pronounced than in the small EC . Such a result suggests that in large EC situations, the values of c_{cr} have a more negative impact on M_{res} .

Furthermore, in Fig. 14b, under the small EC , the mean curve of the SHAP value of EC exhibits some fluctuations but remains relatively dispersed with changes in EC . However, under the large EC , the SHAP value of EC shows a distinct decreasing trend versus EC , signifying that EC has a significant negative impact on M_{res} with an increasing EC .

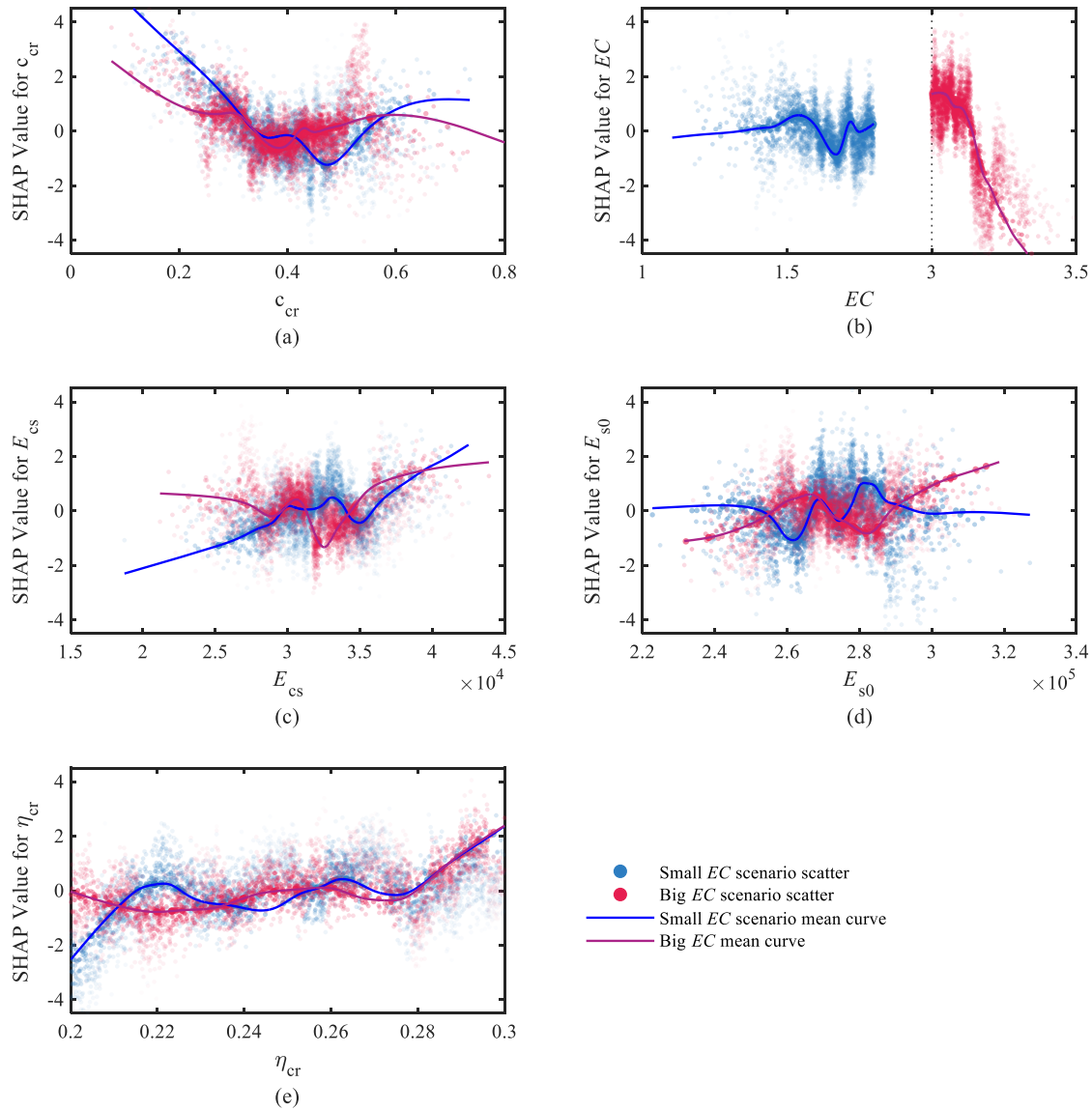


Fig. 14 Feature dependence plots for M_{res} prediction in 10m span scenario under extreme EC s

Additionally, in Fig. 14c, under the small EC , the SHAP value of E_{cs} generally increases with E_{cs} . In contrast, under the large EC , the SHAP value of E_{cs} initially decreases with E_{cs} , then increases after reaching values beyond 35000MPa. In contrast to E_{cs} , Fig. 14d displays that, under the small EC , the SHAP value of E_{s0} exhibits significant fluctuations initially as E_{s0} increases, but under large EC conditions, the SHAP value of E_{s0} generally increases with E_{s0} . Such results indicate that under the small EC , the influence of the concrete elastic modulus on M_{res} increases with the concrete elastic modulus, but under the large EC , the effect becomes more nonlinear. Conversely, the impact of the steel elastic modulus on M_{res} behaves the opposite.

Finally, in Fig. 14e, under the small EC scenario, the SHAP value of η_{cr} initially increases with η_{cr} (for $\eta_{cr} < 0.22$) and then fluctuates. When $\eta_{cr} > 0.28$, its SHAP value increases with η_{cr} . Under the large EC scenario, the SHAP value of η_{cr} exhibits an initial decrease with η_{cr} , followed by fluctuations. Similarly, when $\eta_{cr} > 0.28$, its SHAP value also increases with η_{cr} . It is evident that EC primarily affects the sensitivity of η_{cr} on M_{res} at low values of η_{cr} , while at high values of η_{cr} , it has a positive effect on M_{res} and each effect increases with η_{cr} .

7. Conclusions

This study introduces a three-step ensemble machine learning framework designed to assess the life-cycle performance of RC structures in marine environments, with a specific focus on durability and mechanical properties. The application of this framework is demonstrated through a practical case study involving RC hollow beam bridges in the GBA, China, which were completed in 2020 and consist of three spans. The key conclusions drawn from this investigation are as follows:

1. A time-variant environmental and durability prediction model, tailored for coastal environments, demonstrates strong alignment with historical data from the HKO. Additionally, the results of the chloride transport model are in concordance with in-situ chloride tests conducted in Shenzhen and Hong Kong. These findings validate the efficacy of the proposed model for estimating the life-cycle durability in the GBA.
2. The LightGBM surrogate model attains outstanding precision and training efficiency across all target variables, surpassing alternative methods such as RF, GBDT, XGBoost, and ResNet. Notably, LightGBM accomplishes life-cycle predictions 1000 times faster than conventional simulations, highlighting its substantial efficiency.
3. SHAP analysis reveals the impact of different physical and environmental factors on durability and mechanical predictions. Notably, R_c emerges as the most critical factor affecting $\eta_{ave,ten}$ and $\eta_{ave,com}$, exerting a secondary influence on C_{tc} and M_{res} . Additionally, $D_{c,ref}$ and c_{cr} significantly impact $\eta_{ave,ten}$ and $\eta_{ave,com}$. In the context of 1D chloride transport, c_{cr} initially holds the second position in predicting M_{res} but is later surpassed by other parameters. Conversely, in 2D chloride ion transport, the effects of R_c , c_{cr} , and R_0 on M_{res} become more pronounced over time. These findings underscore the dynamic evolution of feature importance rankings throughout the service life, emphasizing how the significance of various factors in predicting mechanical resistance continually changes.
4. Integrating SHAP plots with the LightGBM model facilitates the assessment of the impact of global warming on the residual bending capacity of RC structures. SHAP plots reveal that c_{cr} , EC , E_{cs} , and E_{s0} display stronger nonlinearity and discreteness in their influence on M_{res} . Under a small EC ($1 \sim 1.8^\circ\text{C}$), the SHAP value of c_{cr} initially decreases with c_{cr} , while under a large EC ($3 \sim 3.5^\circ\text{C}$), this decrease is less pronounced, indicating a greater impact of c_{cr} on M_{res} . The concrete elastic modulus exhibits linear growth in its effects on M_{res} under the small EC but becomes more nonlinear under the large EC , contrasting with the effects of the steel elastic modulus on M_{res} . Moreover, at low η_{cr} , EC primarily influences the sensitivity of η_{cr} on M_{res} , whereas at high η_{cr} values, it has a positive effect, and this effect strengthens with increasing η_{cr} .

In summary, this framework proves to be effective in the assessment of the life-cycle performance of RC structures in marine environments. The framework adeptly captures the dynamic changes in influencing factors, providing engineers with valuable insights into the intricate patterns of performance evolution and influencing factors under diverse climate change scenarios. As a result, it facilitates the implementation of more targeted design and maintenance strategies. While this study assesses the life-cycle durability behaviors of RC structures using a simplified model, future investigations will delve into more comprehensive analyses employing refined and intricate models. These may include a stochastic model for surface chloride deposition and the analysis of various mechanisms such as shear and torsional performance. Additionally, future research should explore diverse machine learning techniques and structural types for comprehensive and multi-scale performance assessments in concrete infrastructure applications.

Acknowledgments

The study has been supported by the Research Grants Council of Hong Kong (PolyU 15225722), the Research Institute for Sustainable Urban Development, the Hong Kong Polytechnic University (PolyU 1-BBWM), the National Natural Science Foundation of China (52078448).

References:

- [1] Guo HY, Jiang C, Gu XL, Dong Y, Zhang WP. Time-dependent reliability analysis of reinforced concrete beams considering marine environmental actions. *Eng Struct* 2023;288:116252. <https://doi.org/10.1016/j.engstruct.2023.116252>.
- [2] Lei X, Dong Y, Frangopol DM. Sustainable Life-Cycle Maintenance Policymaking for Network-Level Deteriorating Bridges with a Convolutional Autoencoder-Structured Reinforcement Learning Agent. *J Bridg Eng* 2023;28:1–15. <https://doi.org/10.1061/jbenf2.beeng-6159>.
- [3] Vinet L, Zhedanov A. A “missing” family of classical orthogonal polynomials. vol. 44. Cambridge University Press; 2011. <https://doi.org/10.1088/1751-8113/44/8/085201>.
- [4] Koch G. Cost of corrosion. Elsevier Ltd; 2017. <https://doi.org/10.1016/B978-0-08-101105-8.00001-2>.
- [5] Markeset G, Rostam S, Klinghoffer O. Guide for the use of stainless steel reinforcement in concrete structures. 2006.
- [6] Gu X-L, Dong Z, Yuan Q, Zhang W-P. Corrosion of Stirrups under Different Relative Humidity Conditions in Concrete Exposed to Chloride Environment. *J Mater Civ Eng* 2020;32:1–8. [https://doi.org/10.1061/\(asce\)mt.1943-5533.0003001](https://doi.org/10.1061/(asce)mt.1943-5533.0003001).
- [7] Gu X, Guo H, Zhou B, Zhang W, Jiang C. Corrosion non-uniformity of steel bars and reliability of corroded RC beams. *Eng Struct* 2018;167:188–202. <https://doi.org/10.1016/j.engstruct.2018.04.020>.
- [8] Stewart MG, Wang X, Nguyen MN. Climate change adaptation for corrosion control of concrete infrastructure. *Struct Saf* 2012;35:29–39. <https://doi.org/10.1016/j.strusafe.2011.10.002>.
- [9] Wang X, Stewart MG, Nguyen M. Impact of climate change on corrosion and damage to concrete infrastructure in Australia. *Clim Change* 2012;110:941–57. <https://doi.org/10.1007/s10584-011-0124-7>.
- [10] Guo H, Dong Y, Gu X. Durability assessment of reinforced concrete structures considering global warming: A performance-based engineering and experimental approach. *Constr Build Mater* 2020;233:117251. <https://doi.org/10.1016/j.conbuildmat.2019.117251>.
- [11] Bastidas-Arteaga E, Schoefs F, Stewart MG, Wang X. Influence of global warming on durability of corroding RC structures: A probabilistic approach. *Eng Struct* 2013;51:259–66. <https://doi.org/10.1016/j.engstruct.2013.01.006>.
- [12] Zhang W, Zhou B, Gu X, Dai H. Probability Distribution Model for Cross-Sectional Area of Corroded Reinforcing Steel Bars. *J Mater Civ Eng* 2014;26:822–32. [https://doi.org/10.1061/\(asce\)mt.1943-5533.0000888](https://doi.org/10.1061/(asce)mt.1943-5533.0000888).
- [13] Guo HY, Dong Y, Gu XL. Two-step translation method for time-dependent reliability of structures subject to both continuous deterioration and sudden events. *Eng Struct* 2020;225:111291. <https://doi.org/10.1016/j.engstruct.2020.111291>.
- [14] Guo HY, Dong Y, Gardoni P. Adaptive subset simulation for time-dependent small failure probability incorporating first failure time and single-loop surrogate model. *Struct Saf* 2023;102:102327. <https://doi.org/10.1016/j.strusafe.2023.102327>.

- [15] Guo HY, Dong Y, Gardoni P. Efficient subset simulation for rare-event integrating point-evolution kernel density and adaptive polynomial chaos kriging. *Mech Syst Signal Process* 2022;169:108762. <https://doi.org/10.1016/j.ymssp.2021.108762>.
- [16] Fu B, Feng DC. A machine learning-based time-dependent shear strength model for corroded reinforced concrete beams. *J Build Eng* 2021;36. <https://doi.org/10.1016/j.jobe.2020.102118>.
- [17] Kumar A, Arora HC, Kapoor NR, Kumar K, Hadzima-Nyarko M, Radu D. Machine learning intelligence to assess the shear capacity of corroded reinforced concrete beams. *Sci Rep* 2023;13:1–26. <https://doi.org/10.1038/s41598-023-30037-9>.
- [18] Ding Z, Zheng S, Lei C, Jia H, Chen Z, Yu B. Machine learning-based prediction for residual bearing capacity and failure modes of rectangular corroded RC columns. *Ocean Eng* 2023;281. <https://doi.org/10.1016/j.oceaneng.2023.114701>.
- [19] Zhang M, Akiyama M, Shintani M, Xin J, Frangopol DM. Probabilistic estimation of flexural loading capacity of existing RC structures based on observational corrosion-induced crack width distribution using machine learning. *Struct Saf* 2021;91:102098. <https://doi.org/10.1016/j.strusafe.2021.102098>.
- [20] Taffese WZ, Sistonen E. Machine learning for durability and service-life assessment of reinforced concrete structures: Recent advances and future directions. *Autom Constr* 2017;77:1–14. <https://doi.org/10.1016/j.autcon.2017.01.016>.
- [21] Machado MR, Karray S, De Sousa IT. Lightgbm: A highly efficient gradient boosting decision tree. *14th Int Conf Comput Sci Educ ICCSE 2019 2019;2017-Decem:1111–6*. <https://doi.org/10.1109/ICCSE.2019.8845529>.
- [22] Lei X, Feng R, Dong Y, Zhai C. Bayesian-optimized interpretable surrogate model for seismic demand prediction of urban highway bridges. *Eng Struct* 2024;301:117307. <https://doi.org/10.1016/j.engstruct.2023.117307>.
- [23] Chen T, Guestrin C. XGBoost: A scalable tree boosting system. *Proc. ACM SIGKDD Int. Conf. Knowl. Discov. Data Min.*, vol. 13-17- Augu, 2016, p. 785–94. <https://doi.org/10.1145/2939672.2939785>.
- [24] Feng DC, Wang WJ, Mangalathu S, Hu G, Wu T. Implementing ensemble learning methods to predict the shear strength of RC deep beams with/without web reinforcements. *Eng Struct* 2021;235:111979. <https://doi.org/10.1016/j.engstruct.2021.111979>.
- [25] Kiani J, Camp C, Pezeshk S. On the application of machine learning techniques to derive seismic fragility curves. *Comput Struct* 2019;218:108–22. <https://doi.org/10.1016/j.compstruc.2019.03.004>.
- [26] Hwang SH, Mangalathu S, Shin J, Jeon JS. Machine learning-based approaches for seismic demand and collapse of ductile reinforced concrete building frames. *J Build Eng* 2021;34:101905. <https://doi.org/10.1016/j.jobe.2020.101905>.
- [27] Xu JG, Hong W, Zhang J, Hou ST, Wu G. Seismic performance assessment of corroded RC columns based on data-driven machine-learning approach. *Eng Struct* 2022;255:113936. <https://doi.org/10.1016/j.engstruct.2022.113936>.
- [28] Ke G, Meng Q, Finley T, Wang T, Chen W, Ma W, et al. LightGBM: A highly efficient gradient boosting decision tree. *Adv Neural Inf Process Syst* 2017;2017-Decem:3147–55.
- [29] Bentéjac C, Csörgő A, Martínez-Muñoz G. A comparative analysis of gradient boosting algorithms. *Artif Intell Rev* 2021;54:1937–67. <https://doi.org/10.1007/s10462-020-09896-5>.
- [30] Lundberg SM, Lee SI. A unified approach to interpreting model predictions. *Adv Neural Inf Process Syst* 2017;2017-Decem:4766–75.

- [31] Lei X, Xia Y, Dong Y, Sun L. Multi-level time-variant vulnerability assessment of deteriorating bridge networks with structural condition records. *Eng Struct* 2022;266:114581. <https://doi.org/10.1016/j.engstruct.2022.114581>.
- [32] Zhang X, Wang L, Zhang J, Liu Y. Bond Degradation–Induced Incompatible Strain between Steel Bars and Concrete in Corroded RC Beams. *J Perform Constr Facil* 2016;30:04016058. [https://doi.org/10.1061/\(asce\)cf.1943-5509.0000921](https://doi.org/10.1061/(asce)cf.1943-5509.0000921).
- [33] Zeng YH, Gu XL, Zhang WP, Huang QH. Study on mechanical properties of corroded prestressed tendons. *Jianzhu Cailiao Xuebao/Journal Build Mater* 2010;13:169–74. <https://doi.org/10.3969/j.issn.1007-9629.2010.02.008>.
- [34] Zhang W, Shang D, Gu X. Stress-strain relationship of corroded steel bars. *Tongji Daxue Xuebao/Journal Tongji Univ* 2006;34:586-592 (In Chinese).
- [35] Guo H, Dong Y. Dynamic Bayesian network for durability of reinforced concrete structures in long-term environmental exposures. *Eng Fail Anal* 2022;142:106821. <https://doi.org/10.1016/j.engfailanal.2022.106821>.
- [36] Costa A, Appleton J. Chloride penetration into concrete in marine environment - Part I: Main parameters affecting chloride penetration. *Mater Struct Constr* 1999;32:252–9. <https://doi.org/10.1007/bf02479594>.
- [37] Liu T, Weyers RW. Modeling the dynamic corrosion process in chloride contaminated concrete structures. *Cem Concr Res* 1998;28:365–79. [https://doi.org/10.1016/S0008-8846\(98\)00259-2](https://doi.org/10.1016/S0008-8846(98)00259-2).
- [38] Vidal T, Castel A, François R. Analyzing crack width to predict corrosion in reinforced concrete. *Cem Concr Res* 2004;34:165–74. [https://doi.org/10.1016/S0008-8846\(03\)00246-1](https://doi.org/10.1016/S0008-8846(03)00246-1).
- [39] Bazant ZP, Sener S, Kim JK. Effect of Cracking on Drying Permeability and Diffusivity of Concrete. *ACI Mater J* 1987;84:351–7. <https://doi.org/10.14359/1739>.
- [40] Bhargava K, Ghosh AK, Mori Y, Ramanujam S. Suggested Empirical Models for Corrosion-Induced Bond Degradation in Reinforced Concrete. *J Struct Eng* 2008;134:221–30. [https://doi.org/10.1061/\(asce\)0733-9445\(2008\)134:2\(221\)](https://doi.org/10.1061/(asce)0733-9445(2008)134:2(221)).
- [41] Bastidas-Arteaga E, Bressolette P, Chateaufneuf A, Sánchez-Silva M. Probabilistic lifetime assessment of RC structures under coupled corrosion-fatigue deterioration processes. *Struct Saf* 2009;31:84–96. <https://doi.org/10.1016/j.strusafe.2008.04.001>.
- [42] Flint MM, Baker JW, Billington SL. A modular framework for performance-based durability engineering: From exposure to impacts. Elsevier Ltd, 2014. <https://doi.org/10.1016/j.strusafe.2014.03.003>.
- [43] Bhargava K, Mori Y, Ghosh AK. Time-dependent reliability of corrosion-affected RC beams - Part 1: Estimation of time-dependent strengths and associated variability. *Nucl Eng Des* 2011;241:1371–84. <https://doi.org/10.1016/j.nucengdes.2011.01.005>.
- [44] Hornbostel K, Larsen CK, Geiker MR. Relationship between concrete resistivity and corrosion rate - A literature review. *Cem Concr Compos* 2013;39:60–72. <https://doi.org/10.1016/j.cemconcomp.2013.03.019>.
- [45] Kivell A, Palermo A, Scott A. Complete Model of Corrosion-Degraded Cyclic Bond Performance in Reinforced Concrete. *J Struct Eng* 2015;141:1–9. [https://doi.org/10.1061/\(asce\)st.1943-541x.0001195](https://doi.org/10.1061/(asce)st.1943-541x.0001195).
- [46] Zhu W, François R. Corrosion of the reinforcement and its influence on the residual structural performance of a 26-year-old corroded RC beam. *Constr Build Mater* 2014;51:461–72. <https://doi.org/10.1016/j.conbuildmat.2013.11.015>.
- [47] China M of T. Specifications for Design of Highway Reinforced Concrete and Prestressed Concrete Bridges and Culverts JTGD62—2004 2004.

- [48] Wang Z, Zeng Q, Wang L, Yao Y, Li K. Corrosion of rebar in concrete under cyclic freeze-thaw and Chloride salt action. *Constr Build Mater* 2014;53:40–7. <https://doi.org/10.1016/j.conbuildmat.2013.11.063>.
- [49] Simpson MJ. Global Climate Change Impacts in the United States. *J Environ Qual* 2011;40:279–279. <https://doi.org/10.2134/jeq2010.0010br>.
- [50] Pang L, Li Q. Service life prediction of RC structures in marine environment using long term chloride ingress data: Comparison between exposure trials and real structure surveys. *Constr Build Mater* 2016;113:979–87. <https://doi.org/10.1016/j.conbuildmat.2016.03.156>.
- [51] Val D V., Trapper PA. Probabilistic evaluation of initiation time of chloride-induced corrosion. *Reliab Eng Syst Saf* 2008;93:364–72. <https://doi.org/10.1016/j.ress.2006.12.010>.
- [52] Saetta A V., Scotta R V., Vitaliani R V. Analysis of chloride diffusion into partially saturated concrete. *ACI Mater J* 1993;90:441–51. <https://doi.org/10.14359/3874>.
- [53] Zhang H, Zhang W, Gu X, Jin X, Jin N. Chloride penetration in concrete under marine atmospheric environment – analysis of the influencing factors. *Struct Infrastruct Eng* 2016;12:1428–38. <https://doi.org/10.1080/15732479.2015.1134588>.
- [54] Bastidas-Arteaga E, Chateauneuf A, Sánchez-Silva M, Bressolette P, Schoefs F. Influence of weather and global warming in chloride ingress into concrete: A stochastic approach. *Struct Saf* 2010;32:238–49. <https://doi.org/10.1016/j.strusafe.2010.03.002>.
- [55] Carnahan B, Luther HA, Wilkes JO. *Applied numerical methods*. Malabar, Fla: Krieger Pub.; 1990.
- [56] Bastidas-Arteaga E, Chateauneuf A, Sánchez-Silva M, Bressolette P, Schoefs F. A comprehensive probabilistic model of chloride ingress in unsaturated concrete. *Eng Struct* 2011;33:720–30. <https://doi.org/10.1016/j.engstruct.2010.11.008>.
- [57] Kwon SJ, Na UJ, Park SS, Jung SH. Service life prediction of concrete wharves with early-aged crack: Probabilistic approach for chloride diffusion. *Struct Saf* 2009;31:75–83. <https://doi.org/10.1016/j.strusafe.2008.03.004>.
- [58] Bhargava K, Ghosh AK, Mori Y, Ramanujam S. Corrosion-induced bond strength degradation in reinforced concrete-Analytical and empirical models. *Nucl Eng Des* 2007;237:1140–57. <https://doi.org/10.1016/j.nucengdes.2007.01.010>.
- [59] ACI committee 318. *Building Code Requirements for Structural Concrete and Commentary (ACI 318M-11)*. vol. 552. American Concrete Inst.; 2011.
- [60] Coronelli D. Corrosion cracking and bond strength modeling for corroded bars in reinforced concrete. *ACI Struct J* 2002;99:267–76. <https://doi.org/10.14359/11910>.
- [61] Zhang WP, Chen H, Gu XL. Bond behaviour between corroded steel bars and concrete under different strain rates. *Mag Concr Res* 2016;68:364–78. <https://doi.org/10.1680/jmacr.15.00174>.
- [62] Gu X, Jin X, Zhou Y. *Basic Principles of Concrete Structures*. 2016. <https://doi.org/10.1007/978-3-662-48565-1>.
- [63] Helton JC, Davis FJ. Latin hypercube sampling and the propagation of uncertainty in analyses of complex systems. *Reliab Eng Syst Saf* 2003;81:23–69. [https://doi.org/10.1016/S0951-8320\(03\)00058-9](https://doi.org/10.1016/S0951-8320(03)00058-9).
- [64] He K, Zhang X, Ren S, Sun J. Deep residual learning for image recognition. *Proc. IEEE Comput. Soc. Conf. Comput. Vis. Pattern Recognit.*, vol. 2016- Decem, 2016, p. 770–8. <https://doi.org/10.1109/CVPR.2016.90>.